Citation for published version:
Chandrasekaran, S, Bowen, C, Zhang, P, Li, Z, Yuan, Q, Ren, X & Deng, L 2018, 'Spinel photocatalysts for environmental remediation, hydrogen generation, CO2 reduction and photoelectrochemical water splitting', Journal of Materials Chemistry A, vol. 6, no. 24, pp. 11078-11104. https://doi.org/10.1039/C8TA03669A

DOI:
10.1039/C8TA03669A

Publication date:
2018

Document Version
Peer reviewed version

Link to publication

University of Bath

General rights
Copyright and moral rights for the publications made accessible in the public portal are retained by the authors and/or other copyright owners and it is a condition of accessing publications that users recognise and abide by the legal requirements associated with these rights.

Take down policy
If you believe that this document breaches copyright please contact us providing details, and we will remove access to the work immediately and investigate your claim.

Download date: 31. May. 2019

Spinel photocatalysts for environmental remediation, hydrogen generation, CO_2 reduction and photoelectrochemical water splitting

Sundaram Chandrasekaran[a,b], Chris Bowen[c], Peixin Zhang[a], Zheling Li[d], Qiuhua Yuan[a], Xiangzhong Ren[a], and Libo Deng[a]*

[a]College of Chemistry and Environmental Engineering, Shenzhen University, Shenzhen 518060, China

[b]Key Laboratory of Optoelectronic Devices and Systems of Ministry of Education and Guangdong Province, College of Optoelectronic Engineering, Shenzhen University, Shenzhen 518060, China

[c]Department of Mechanical Engineering, University of Bath, BA2, 7AY, Bath, UK

[d]National Graphene Institute and School of Materials, University of Manchester, Manchester, M13 9PL, UK

* *Corresponding author:*

Libo Deng: Denglb@szu.edu.cn

Abstract

Over the past few decades, owing to the unique functional properties such as physical, chemical, optical and electronic properties, the spinel materials have attracted significant scientific attention in heterogeneous photocatalysts research. Here, we review the main fundamental understanding of the correlations between the performance of spinel structures and their particle shape, size, chemical composition, and photo-Fenton reactions for photocatalytic applications; these include photocatalytic dye degradation for environmental remediation, photocatalytic hydrogen generation, CO_2 reduction and photoelectrochemical water splitting. In addition, the key factors and essential strategies to improve their performance and functionality are discussed in detail. Future research pathways and perspectives on the progress of these high performance and cost effective renewable energy materials are provided, along with the improvements in materials properties that are necessary to replace current commercial energy materials. It is envisioned that further investigations should focus on surface modification, integrating conductive matrixes and regulating of the spinel composition, which will make spinels promising photocatalysts.

Keywords: Spinels, metal oxides, photocatalysts, dye degradation, CO_2 reduction, water splitting.

Introduction

Energy conversion and storage have attracted significant scientific and engineering interest as an important step to efficiently use clean and renewable energy, in particular for intermittent energy supplies, [1, 2]. As a green and promising technology, energy conversion using semiconducting metal oxide photocatalysis has the potential to utilize clean and naturally abundant sunlight as an energy source, for the remediation of environmental pollutants by degradation and clean energy generation such as hydrogen (H_2) and oxygen (O_2) production from water and reduction of carbon dioxide (CO_2)[3]. Recently these materials have led to extensive interests in the fields of energy materials and environmental chemistry.[4-8] Approximately 60 years ago, the photocatalytic activity of titanium dioxide (TiO_2) was reported by Markham[9]. However, a seminal note published in Nature in 1972 by Fujishima and Honda[10] led to remarkable progress with respect to the potential of titania for water splitting, which is a potential candidate due to its photoactive properties, low cost, and durability. However, the wide band gap of TiO_2 limits its use to harvest the ultraviolet (UV) region only. In order to harvest whole solar spectrum including UV and visible regions, several types of semiconducting metal oxides have been examined, including d^0 and d^{10} metal configurations based oxides, plasmonic materials, sulfides, nitrides , oxy-nitrides and etc[11-14]. To date, no photocatalytic material completely fulfills all the practical necessities for successful operation which include high durability, optimum narrow band gap for full utilization of the complete solar spectrum, long lifetime of photo-generated electron–hole pairs, low cost, eco-friendly nature, high efficiency and stability [15]. Hence, it is utmost essential to develop well-organized and visible-light-driven photocatalytic materials with long term durability *via* optimizing existing synthesis strategies

through coalescing the photocatalyst with low cost metal or metal oxide co-catalysts, and fashioning appropriate heterojunctions[16, 17]. Normally, the strategies to modify heterogeneous photocatalysts for enhanced activity include structural and chemical compositional optimization[18, 19]. The photocatalytic chemical reactions for heterogeneous photocatalysis occur mainly at the surface of the semiconductor material. The photocatalytic properties of semiconducting materials are highly reliant on their crystalline structure and nanometer sized structural features[20, 21]. Thus, the optimization and control of the structural properties of a known metal oxide semiconductor is essential to enhance photocatalytic activity. Till date, a number of promising nano- and micro-sized material structures and structural engineering approaches have been proposed to create efficient photocatalytic systems[22, 23].

One interesting class of material that have the potential to meet these challenges include nanostructured spinel oxides which include *normal* and *inverse* spinels, which have been shown to fulfill the demands described above. Compared to other materials, the spinels revealed potential benefits of high energy density, and thus the spinel structured materials have attracted great attention in energy conversion and storage applications[24]. This interest originates from their ease of fabrication and their structural, physical and chemical properties can be readily tuned and optimized for a desired application. This can lead to low cost, efficient, eco-friendly, and versatile material systems for solar water splitting and environmental remediation (such as dye degradation)[17, 25].

Notably, the mesoporous nature associated with large surface area of hierarchical spinel structured low band gap photocatalysts are beneficial to improve (i) the light harvesting efficiency (ii) the rate of adsorption of reactants and (iii) to ease the transport of guest species to the binding sites, as shown in **Fig. 1**. With these features, to date, a great variety of reports have described the fabrication

of spinel materials with manifold porous structures and enhanced efficiency. Despite some excellent reviews devoted to spinels, only a small portion refer to their preparation and applications in photocatalysis[17, 26], photoelectrochemistry[27, 28] and environmental remediation[29]. Thus, we believe that, a broad and inspiring appraisal on this subject is timely to promote further growth in this significant, stimulating and emerging area of spinels, photocatalysts and environmental remediation research.

In this comprehensive review, we summarize recent progresses in the area of nanostructured spinel materials for a range of photocatalytic applications. A distinct emphasis of the review is that it aims to provide a better understanding of the fundamental design, fabrication, mechanisms, performance and applications of both spinel oxides for photocatalytic applications; including the normal and inverse spinels. The advantages of the structural differences in spinel oxides are initially discussed in the context of spinel oxide based photocatalysis. The strategies to enhance the performance of spinels are then presented. We will review the various applications with consistent mechanisms of the spinel photocatalysts for degradation of pollutants, H_2 production, CO_2 reduction and photoelectrochemical (PEC) water splitting. Finally, the future research challenges to improve the efficiency of the material systems are discussed.

2. Types and significance of spinels

Depending on the nature of the crystalline structures, the spinels are classified into two types, namely the normal (or regular) spinels and inverse spinels.

2.1. Normal or Regular Spinel Structures

Normal spinel structures have the general element formula of AB_2X_4, where A and B in the spinel structures can be divalent and trivalent (or tetravalent) cations respectively[30], for instance A site represents the atom that has a valence of two including any one metal ions such as Cu(II), Zn(IV), Cd(IV), Mg(IV), Ni(IV), Co(IV), Fe(IV), Mn(IV), Ba(VI), Ca(VI) etc.; and B

site represents the atom that has a valence of three including any one metal ions such as Ga(VI), In(VI), Cr(VI), Mn(VI), Al(VI), Zn(VI), Sn(IV) etc. Typically, octahedral interstices are larger than the tetrahedral sites. Thus, smaller radii cations prefer to occupy the A sites, whereas larger radii cations prefer to occupy B, i.e. simply, A and B are tetrahedrally and octahedrally coordinated cations in the spinel structure, respectively. Moreover, X can be either a chalcogenide or oxide. In the regular (normal) spinel structures, the anions are arranged in close-packed arrays, as shown in **Fig. 2**. During the formation of the spinel, the A-site cations fill 1/8 of the tetrahedral holes and the B-site cations fill 1/2 of the octahedral holes; where the divalent A^{II} ions fill the tetrahedral spaces and the trivalent B^{III} ions fill the octahedral spaces in a close packed arrangement of oxide ions. A regular spinel structure can be denoted as: $(A^{II})^{tet}(B^{III})_2{}^{oct}O_4$, e.g. $ZnFe_2O_4$, Mn_3O_4, $FeCr_2O_4$ (chromite) or $MgAl_2O_4$.

2.2. Inverse spinels

The inverse spinel structures are described by $(B(AB)O_4)$, where the divalent A^{II} cations fill the octahedral voids (i.e valance two metals), and half of B^{III} ions (i.e valance three metals) fill the tetrahedral voids. This spinel structure can be written as: $(B^{III})^{tet}(A^{II}B^{III})^{oct}O_4$, such as Fe_3O_4 (ferrite), $CoFe_2O_4$, or $NiFe_2O_4$. The inverse spinel structures can also be denoted as: $CoFe_2O_4 = Fe^{III}(Co^{II}Fe^{III})O_4$, $Fe_3O_4 = Fe^{III}(Fe^{II}Fe^{III})O_4$ or $NiFe_2O_4 = Fe^{III}(Ni^{II}Fe^{III})O_4$. In the inverse spinel structure, the number of octahedral sites occupied can be well-ordered or random, where the random occupation of cations leads to spinel defects in the structure. For example, $NiAl_2O_4$ can be written as $(Al_{0.75}Ni_{0.25})^{tet}$ $[Ni_{0.75}Al_{1.25}]^{octa}O_4$; another example of a defected spinel is γ-Al_2O_3. The spinel structures of magnetic iron oxide nanoparticles have long been of scientific and technological importance. The cubic spinel structured MFe_2O_4, or $MO{\cdot}Fe_2O_3$, represents a well-known and important class of iron oxide materials where oxygen forms a face centered

cubic close packing, and M^{2+} and Fe^{3+} occupy either tetrahedral or octahedral interstitial sites. By adjusting the chemical identity of M^{2+}, the magnetic configurations of MFe_2O_4 can be engineered to provide a wide range of magnetic properties. Depending on the M^{2+} cations (where M = Co, Li, Ni, Zn, etc.)[31, 32], the spinels can either have high magnetic permeability and electrical resistivity or half-metallicity (for M = Fe)[33, 34]. For instance, bulk $ZnFe_2O_4$ exhibiting *normal spinel* structure is a weak anti-ferromagnetic behavior with ~ 10.5 K Neel-temperature[35, 36], whereas epitaxial $ZnFe_2O_4$ thin films reveal a higher Neel temperature about ~ 43 K [37]. However recent investigates disclose that nanocrystalline $ZnFe_2O_4$ shows ferrimagnetic behavior with *partial inversion of the spinel* structure[38], i.e. the extra occupation of tetrahedral A sites by Fe and octahedral B sites by Zn are most significant to a strong super exchange pairing of the intra sublattice of Fe ions[39, 40]. Thus, the $ZnFe_2O_4$ nanoparticles are responsible for the hysterics loop upon magnetization reversal. For easy comparison, the structural classifications are presented in **Table 1**.

2.3 Photocatalytic and PEC Mechanisms

Typically, there are four familiar types of photocatalysis, specifically (i) plant photosynthesis (ii) microalgae photosynthesis (iii) photocatalysis by suspension and (iv) photoelectrochemical analysis or photoelectrocatalysis using photoelectrodes. Complete investigations of photocatalysts and assimilated photocatalytic schemes have been used to shed light on the dissimilar work functions of each constituent in an operational photocatalyst. Mainly, pollutant degradation and energy conversion by photocatalytic materials is of significant practical interest, and extensive research efforts have been devoted to advance novel photocatalysts to enhance the efficiency, especially under visible light. Photocatalysis is a process in which the light absorption by a photocatalytic material results in the generation of photogenerated electrons and holes, which is then

transported to other molecules at the surface of the photocatalyst. During this photocatalytic reaction, if the reduction-oxidation (redox) potential lies below the conduction band (CB) of the photocatalytic material, the electron can be transported to an acceptor molecule, whereas the hole can be transported to a donor if its redox potential lies above the valance band of the photocatalyst. A schematic of the photocatalytic mechanism is presented in **Fig. 1**. As an example, the stages typically involved in a photocatalytic reaction process are (i) generation of electron-hole pairs by light absorption (ii) separation of excited charge (iii) electrons and holes transfer to the photocatalyst surface (iv) electron and hole recombination and (v) use of charges on the surface for redox reactions.

One of the least complex applications of photocatalysis is to simply suspend a photocatalysts in an electrolyte solution and expose it to light. The photocatalysts are mostly nanosized and/or micro photocatalyst materials which can be considered as an integrated system consisting of photoanode and/or photocathode for a photo-electro-chemical (PEC) system. In PEC system, the oxidation and reduction are the basic electrochemical reactions that occur during water splitting. Primarily, when a PEC semiconductor photoelectrode device with the well-defined set of functional properties is immersed in an electrolyte solution and irradiated to light, the photon (light) energy is converted into electrochemical energy that can split water into hydrogen (H_2) and oxygen (O_2). For excellent H_2 and O_2 evolution reactions, the positions of conduction band (CB) and valance band (VB) of the semiconductor photoelectrode are required to fit into the water reduction and oxidation potential region, respectively. Upon light irradiation, the excited electrons favor the hydrogen generation, whereas the oxygen is generated by holes.

The overall solar water splitting includes two half reactions taking place at the photoanode and/or photocathode instantaneously, as detailed below:

$$2H_2O + h\upsilon \rightarrow 2H_2 + O_2 \quad (1)$$

$$4\,H^+ + 4\,e^- \rightarrow 2H_2 \quad (2)$$

$$2H_2O \rightarrow 4\,H^+ + 4\,e^- + O_2 \quad (3)$$

It is well documented that, nanostructured spinel catalysts are potentially alternative materials to noble metal catalysts due to their low cost, enhanced activity at low temperature, eco-friendly nature, abundance and resistance to poisoning. For environmental concern aspects, the major chemical wastes of hazardous materials from industries were found to affect aquatic and human life. Hence, it is enforced to develop cost effective and environmental friendly methods to remove them from aqueous solution. Most effective pathway is to use spinel photocatalytic materials to solve this environmental problem.

3. Photocatalytic environmental remediation by Spinels

The contamination of water resources by a range of potentially toxic dyes from industrial wastes such as plastic, paper, leather, cosmetics, chemicals and textiles has been considered an ecological problem. Many dyes used by commercial industries are synthetic complexes of aromatic molecules, which are highly stable pollutants and challenging in terms of achieving biodegradation. In this regard, dye degradation by photocatalytic processes have been widely explored by TiO_2-based materials under UV irradiation[41, 42]. However, a disadvantage of TiO_2 for this application is that it is active only in UV light illumination due to its wide band gap; it is impotent to harvest the incoming whole solar spectrum fully. In order to overcome this issue, photocatalytic materials of metal oxide semiconductors are considered to be an alternative and environmentally benign approach. Various semiconductors have been verified as photocatalysts due to their photo-stability, non-toxicity, ease of use and low cost[43,18, 44]. Among them, Gahnite ($ZnAl_2O_4$) is a face-centered cubic spinel-structured oxide, which has good chemical and thermal stability, large mechanical resistance and short surface acidity. In

2014, Battiston et al.[45] reported the synthesis of $ZnAl_2O_4$ by co-precipitation. The photocatalytic activity was assessed by the organic pollutant degradation (direct black 38 dye) in an aqueous solution under sunlight. Owing to its good thermal stability, the mesoporous zinc aluminate ($ZnAl_2O_4$) particles exhibited an enhanced photocatalytic degradation activity at an initial concentration of ~ 80 mg L^{-1}, which has been further verified by other research groups[46, 47].

Later, another class of metal oxides, the spinel ferrites (MFe_2O_4), capable of utilizing a major portion of the incoming solar spectrum, was studied due to their energy gap being appropriate for absorbing visible light, see **Table 1.** These spinels are attractive for photocatalytic reactions due to the spinel nature and their exceptional optical, chemical and electrical properties. For example, Zhang et al.[48] reported the production of radical species from peroxymonosulfate (PMS) using $CuFe_2O_4$ spinel. A strong pollutant of iopromide was used as a model system and during the reaction, as a result of its crystalline nature, $CuFe_2O_4$ exhibited a greater activity of ~1 mol/mol for oxalate degradation and it exhibited about ~ 30 times lower Cu^{2+} leaching (1.5 μg L^{-1} per 100 mg L^{-1}) than a well-crystallized CuO at the same dosage, as shown in **Fig 3**. The radical of sulfates were described as the primary radical species responsible for the iopromide degradation.

3.1 Reaction kinetics of spinel photocatalysts

The understanding of reaction kinetics and mechanism of the photocatalytic activity is essential to enhance the performance. It is well known that, photocatalytic oxidation and/or reduction have the benefit that habitually converts pollutants in water, carbon dioxide and inorganic materials through facile way. Usually, during photocatalytic reactions, when photocatalyst absorbs illuminated radiation from sun or light source, it will create pairs of electrons and holes on its surface. The valance band electron of the photocatalysts becomes

excited when illuminated by light. The excess energy of this excited electron encouraged the electron to the conduction band of photocatalysts, thus generating the negative-electron (e^-) and positive-hole (h^+) pair. The positive-hole of photocatalysts breaks apart the water molecule (or waste products, toxins and pollutants) to produce hydrogen gas and hydroxyl radical. The negative-electron reacts with oxygen molecule to create super oxide anion. This reaction cycle persists when light is available. The possible products during the photocatalytic activity are shown in the following equations:[49-51]

$$AB_2O_4 + h\upsilon \rightarrow AB_2O_4 (h^+_{VB}) + AB_2O_4 (e^-_{CB}) \quad (4)$$

$$O_2 + AB_2O_4 (e^-_{CB}) \rightarrow O_2.^- \quad (5)$$

$$O_2.^- + H^+ \rightarrow HO_2. \quad (6)$$

$$HO_2. + O_2.^- \rightarrow HO_2^- + O_2 \quad (7)$$

$$2HO_2. \rightarrow O_2 + H_2O_2 \quad (8)$$

$$H_2O_2 + h\upsilon \rightarrow 2OH. \quad (9)$$

$$H_2O_2 + e^-_{CB} \rightarrow OH^- + OH. \quad (10)$$

These are the basic reactions that can be useful to increase the photocatalytic activity through the understanding of reaction mechanisms. In Equation (4), "A" represents the divalent and "B" represents the trivalent (or tetravalent) cations. In addition, the spinel-type compounds of zinc chromite ($ZnCr_2O_4$)[52] and zinc aluminate ($ZnAl_2O_4$)[53] were successfully used for the removal of dyes from wastewater via photocatalytic processes. The basic photocatalytic mechanism of $ZnCr_2O_4$ was described by the following equations:

$$ZnCr_2O_4 + h\upsilon \rightarrow h^+ + e^- \quad (11)$$

$$h^+ + OH^- \rightarrow OH^{\cdot} \text{ (hydroxyl radicals)} \quad (12)$$

$$OH^{\cdot} + {}^{\cdot}O_2^- \text{ (active oxygen species)} + \text{organic substances (such as dyes)} \rightarrow CO_2 + H_2O \quad (13)$$

Moreover, the band gap of $ZnCr_2O_4$ was estimated to be ~ 3.35 eV and ~ 3.96 eV by UV-visible and luminescence spectroscopy respectively[54]. This makes this particular material only responsive to UV light irradiation, as with the TiO_2 band gap (~ 3.2 eV). The wide band gap of $ZnCr_2O_4$ can be more active under ultraviolet (UV) irradiation (λ<387 nm), but this represents only ~ 5% of the total solar energy. Therefore, doping of the material with transition-metal cations or organic materials, such as graphene, is necessary to extend its activity when illuminated by visible light. Among the various ferrites, $MgFe_2O_4$, a member of spinel family, has a wide range of applications including electronic devices, heterogeneous catalysis, and sensor technologies[55]. The excellent physical and chemical behavior of the ferrite spinels makes it a favorable candidate for photocatalytic applications. A number of studies on the photo oxidation of methylene blue in aqueous solution using $MgFe_2O_4$ powder irradiated with UV (350 nm) and visible-light (>420 nm) and photo-electro-chemical water splitting experiments under visible light have been reported[56].

The photocatalytic degradation mechanism of organic based impurities by semiconducting $MgFe_2O_4$ is the same as Equation (4). In this reaction, the semiconductor materials (e.g. $MgFe_2O_4$, $ZnFe_2O_4$, $ZnCr_2O_4$, etc.,) initially absorbs incident light and, as a result of photo excitation, an electron–hole pair is produced at the surface of the semiconducting photocatalyst; see Equations (4) and (11). During the photocatalytic dye degradation process, the high oxidation potential of the holes (h^+_{CB}) leads to the direct oxidation of the organic matter (such as a dye) and reactive and/or volatile intermediates are produced through the following route (Equation 14):

$$h^+_{(VB)} + \text{dye} \rightarrow \text{dye}^{\bullet+} \rightarrow \text{dye oxidation} \qquad (14)$$

Then, hydroxyl radicals (i.e. highly reactive species) can also be produced by either

breakdown of H_2O (Equation 15) or by reacting hydroxyl ion (OH^-) with a hole (Equation 16)[2, 57].

$$h^+_{(VB)} + H_2O \rightarrow H^+ + \cdot OH \quad (15)$$

$$h^+_{(VB)} + OH^- \rightarrow \cdot OH \quad (16)$$

During the above reactions, the produced hydroxyl radicals are usually highly oxidant and non-specific with the redox potential of $E_0 \sim +3.06$ V. If the hydroxide radicals react with the organic compounds, incomplete or complete mineralization of the organic compounds can occur. Further, superoxide anions are also produced by the reduction of oxygen molecules (Equation 10), which can take place by the presence of electrons in the conduction band at the photocatalyst surface. Then, the existence of organic based scavengers lead to the creation of organic peroxides or hydrogen peroxide molecules with the use of radical peroxide anions. From these reactions it was confirmed that the conduction band electrons are also responsible for the generation of radicals of hydroxyl species, which have been validated as the main cause of organic complexes degradation.

In contrast, it was found that for spinels of $MgFe_2O_4$ and $ZnFe_2O_4$, and orthorhombic $CaFe_2O_4$, the photocatalytic activity was found to be affected by the surface area and crystallinity of the photocatalyst[58]. Also, it was evidenced that the spinel structured materials are promising candidates for a range of applications[59] including sustainable hydrogen production, catalysis, and electronic and magnetic device fabrications. Later, copper, cobalt, nickel, zinc and several mixed-metal and core–shell spinels have been applied in catalytic reactions[60]. Most of them belong to photo-Fenton process, which is now discussed below.

3. 2 Photo-Fenton process on spinels

In the 1890's, Henry John Horstman Fenton developed a Fenton's reagent. This solution

contains a catalyst of iron (Fe) with hydrogen peroxide (H_2O_2) for environmental remediation and is used to oxidize pollutants or waste waters[61]. Fenton's reagent can be used to remove organic compounds such as trichloroethylene (TCE) and perchloroethylene (PCE). During the reaction, Fe^{2+} is oxidized by H_2O_2 into Fe^{3+}, forming a hydroxyl radical and hydroxyl ion. Furthermore, the Fe^{3+} ion is then reduced back to Fe^{2+} by hydrogen peroxide, forming a hydroperoxyl radical and a proton as shown in the reactions below:

$$Fe^{2+} + H_2O_2 \rightarrow Fe^{3+} + HO\bullet + OH^- \quad (17)$$

$$Fe^{3+} + H_2O_2 \rightarrow Fe^{2+} + HOO\bullet + H^+ \quad (18)$$

Nowadays, photo-Fenton reactions have been advanced, which have the potential for degradation of toxic chemicals, and have been considered in the presence or absence of ligands, which have been complexed to Fe(II) or Fe(III). Among the various materials, ferrite based spinel photocatalysts has attracted attention since its heterogeneous nature and iron (Fe) offers the possibility for catalyst reuse and ferrite catalysts can enrich the oxidizing power of photo-Fenton type reactions. Spinels are environmentally benign, inexpensive, and abundantly available. As an extremely stable metal oxide photocatalyst with a narrow band gap, it has the potential to harvest the whole solar spectrum to degrade a variety of toxins and contaminants. This significant feature favors the development of photocatalytic process of spinels for advancing an efficient photochemical system for purification of water and air[62].

It is well-known that combining photocatalysts in different mixtures and ratios leads to variable results, which are subject to the conditions used[17]. The photocatalytic materials utilize photon energy (*hv*) to execute oxidation and reduction reactions. When photocatalytic activity occurs in aqueous solutions, water (H_2O) and hydroxide ions (such as NaOH, KOH and etc.) react with photo generated h^+ to generate hydroxyl radicals ($^{\cdot}OH$); see Equations 15 and 16. The

process of generating hydroxyl radicals can occur through two pathways; initially the oxygen (O_2) present in water is reduced to form $O_2^{\cdot -}$, which then reacts with hydrogen (H^+) to form **.**OOH, followed by rapid decomposition to **.**OH. The second pathway involves the oxidation of OH^-. During this reaction the band gap of the photocatalyst determines the wavelength of light energy that can be absorbed. In this case, spinel ferrites are recognized to be effective photocatalysts and it was reported[63] that ferrites can be effective in Fenton-type systems at neutral to basic pH and the $MnFe_2O_4$, $CuFe_2O_4$, $CoFe_2O_4$, and Fe_3O_4 spinels exhibited the production of **.**OH from H_2O_2 at pH = 4-8. In some cases the effective pH range can be extended further and depends on the chemical composition, for instance $CuFe_2O_4$ and $CoFe_2O_4$ are able to generate **.**OH at pH = 12 whereas this happens for $MnFe_2O_4$ at pH = 2. This is a significant progress over the normal restrictive acidic conditions needed (pH = 2–4) for a classical Fenton system. Arifin et al.[64] examined the solar thermal splitting CO_2 cycle using nanosized $CoFe_2O_4$ and $FeAl_2O_4$ spinels. It was observed that the CO_2 oxidation kinetics was slightly slower than the O_2 oxidation kinetics in $CoFe_2O_4$-coated Al_2O_3 system.

Recently, Fenton-like nano-photocatalysts of Pt coupled $ZnFe_2O_4$ was reported by Kuan-Ting Lee et al[65]. This photocatalyst shortened the photo degradation treatment time for Rhodamine B (RhB) to seconds from hours when exposed to visible light. The maximum reaction rate constant was 9.31 min^{-1} (where the RhB concentration was ~ 5 ppm). In addition, the magnetic behavior is another benefit of spinel ferrite photocatalysts, which makes these materials easy to recover from the catalytic systems after the reaction finished, which is particularly useful for facile recycle of the catalyst.

Normally, the spinel structures allow different metallic ions to enter into its host lattice, thus modifying the structural, chemical, electrical and catalytic properties. The sharing of cations

over the tetrahedral and octahedral sites is influenced by several factors such as substituent ion size, charge influenced by the substituent ion, atomic site preference of the substituent ion, synthetic strategy, conditions and the amount of substitute ions. A number of publications have reported the alteration of spinels via different methods[66-70] to enhance the activity and performance of the final spinel materials[71]. In the morphology controlled aspects, compared with nanosphere and flower shaped $ZnFe_2O_4$ spinels, the one dimensional $ZnFe_2O_4$ porous nanorod with a diameter of 60 nm showed excellent photocatalytic degradation of Safranine-O (SO) and anionic Remazol Brilliant Yellow (RBY) dyes[72]. The enhanced photoactivity was mainly due to the narrow band gap, as well as the nano-voids present in the assembled 1D nanorods which resulted in a porous structure with a high specific surface area. Besides, micropeony structured $ZnIn_2S_4$ spinel was also used to degrade methylene blue (MB)[73]. The micropeony showed a diameter of ~ 1.94 μm with the pedals thickness of ~10 nm. This peony structure revealed high surface area with specific benefit to prevent the composition of electron-cavity and thus improved the photocatalytic activity. As a result, 99.98% MB dye degradation was observed at ~ 90 min for nano/micropeony structured $ZnIn_2S_4$. It was observed that these structural features might fetch stronger absorbability and better photocatalytic reaction activity that increase the dye degradation efficiency. Also, photocatalysts of mixed-metals[74-76] and heterostructures of core–shell spinels[77-79] were used to enhance the dye degradation efficiency.

Recently, the spinel photocatalysts have been gaining particular research attention due to their unique structural, optical and catalytic properties. However, owing to the wide band gap, some spinel photocatalysts are still poor in visible light region and low electron - hole charge separation efficiency. In order to enhance the photocatalytic activity, the fundamental understanding of chemical physics behind the spinels is crucial. Likewise, the appropriate choice

of synthesis method and selecting the appropriate materials for intrinsic doping such as carbon materials and/or other metals will control the particle size, band gap, optimum chemical composition with well-defined crystalline nature and also the morphology, thereby enhancing the performance of the final photocatalyst (*see section 7*).

4. Clean energy generation by Spinels

4.1. Hydrogen production by spinel photocatalysts

Photocatalytic hydrogen (H_2) evolution by direct water splitting or by using sacrificial agents and carbon dioxide (CO_2) reduction are of interest in the energy conversion process. In a simplified form of water splitting, H_2O is being reduced and oxidized at the same time, producing an oxidized product of O_2 and reduced product of H_2. Typically, it is common to introduce sacrificial reagents that would either afford electrons or holes to facilitate the overall water splitting reactions. Recently, highly active electrocatalysts as co-catalysts have been recognized as an effective method to reduce the overpotential of water splitting; namely the splitting of H_2O into H_2 and O_2 in a stoichiometric ratio of 2 : 1 under light illumination in the existence of a photocatalyst. In this aspect, a number of different metal oxide photocatalysts have been investigated[80-83]. However, the efficiency of photocatalytic water splitting for practical application is typically low due to the need to overcome some important obstacles such as efficiency and long term durability. On the other hand, H_2 production efficiency can be enhanced using high cost sacrificial agents (such as alcohols and glycerol etc.,)[82]. Hence, the research community has been recently focusing on spinels, since they have relatively narrow band gap, large surface area, are easy to fabricate and are cost effective. To improve the efficiency for photocatalytic hydrogen production, methodologies similar to those for other photocatalysis applications have been used for spinels, namely the porosity and surfacea, optimization of the crystallinity, doping, and

heterostructures [84].

Lu et al.[85] reported on hydrogen generation by H_2S photodecomposition on a $ZnFe_2O_4$ photocatalyst. The system was consisted of a dispersed photocatalysts, which was irradiated with visible light and under different conditions. As a result, a high rate of hydrogen generation around ~ 0.025 ml h^{-1} mg^{-1} was perceived. In that study, the dependences of H_2 production rate on solution pH and sulfide concentration were also studied, remarkably the $ZnFe_2O_4$ spinel powder showed an excellent performance for H_2S photodecomposition at pH = 8-12. Dom et al.[86] prepared $ZnFe_2O_4$ spinels by various methods such as solid state reaction (SSR), polymer complex (PC), microwave sintering (μW) and self-propagating combustion (SPC) method, as shown in **Fig 4**. As a consequence, a more negative flat band potential of ~ -0.543 *vs*. NHE and high quantum yield of ~ 0.19% for hydrogen evolution was observed for the microwave sample, i.e. $ZnFe_2O_4$ prepared from the microwave sintering method showed the best performance.

In addition, the photocatalytic H_2 evolution of CuM_2O_4 (where M=Al, Cr, Mn, Fe and Co) spinel was also examined[87]. These spinel oxides exhibited p-type semiconducting nature, which was confirmed by positive thermopowers and low onset photocurrents. Furthermore, it was revealed that electron jumping between similar sites resulted in a normal spinel with low activation energy; however larger energies were observed for inverse spinel. Owing to this features, the $CuCo_2O_4$, $CuFe_2O_4$ and $CuMn_2O_4$ photocatalysts showed high efficiencies of ~ 0.098%, ~ 0.100% and ~ 0.100%, respectively in 1 M KOH under a 200W tungsten lamp. This enhanced activity was dependent on the synthetic condition and band bending effect of spinels. Also, the enhanced photocatalytic activity was interpreted in terms of electronegativity and flat band potential and the existence of cobalt in the spinel structure was the reason for the raised affinity of electrons. In addition, two narrow band gap spinel structured semiconductors

$CuMn_2O_4$ and $ZnMn_2O_4$ were testified[88] for hydrogen generation by visible light in aqueous solution containing sulfite SO_3^2 or sulfide S^{2-}. The platinized $CuMn_2O_4$ showed an enhanced H_2 evolution rate, of about ~ 2.6 $\times 10^{-3}$ ml $mg^{-1}h^{-1}$ in a 0.1M SO_3^{2-} alkaline solution, where platinum was used as a counter electrode and sulfide was used as hole scavenger. Remarkably, the H_2 production rate was decreased over time and attained a zero value after 3h; this was mainly due to the development of colored polysulfides S_n^{2-}. Moreover, the energy gap of $FeCr_2O_4$ is ~ 1.33 eV, which is lower than the driving force needed for water splitting[89,90] In aqueous electrolytes, the best photo response for H_2 production was acquired in a S^{2-} solution with an evolution rate of ~ 8.26 cm^3 g^{-1} h^{-1}. Furthermore, for a comparative analysis, the photocatalytic activity of unreduced $FeCr_2O_4$ used towards water–gas shift reaction (i.e. $CO + H_2O \rightarrow CO_2 + H_2$) at various temperature ranges from 523–723 K, were examined. As a result, the rate of H_2-production and the CO conversion of about ~ 280 μmol g^{-1} s^{-1} and 44% respectively at 723 K was perceived.

A range of nanostructured spinels have been examined with enhanced photocatalytic performance for hydrogen production under light illumination. Cubic spinel of $CdIn_2S_4$ with marigold-like and nanotube structured samples were prepared by a simple hydrothermal method[91]. Both samples exhibited good chemical stability. The aqueous and methanol mediated $CdIn_2S_4$ products displayed outstanding photocatalytic activity with quantum yields of 16.8 % (for a marigold-like structure) and 17.1 % (for nanotubes) at 500 nm, respectively, for H_2 evolution under visible light. This enhanced performance was accredited to the well-defined crystalline nature and band structure of $CdIn_2S_4$.

Typically, for H_2 generation by photocatalytic experiments, alcohols are used as a sacrificial reductant to donate electrons. Such methodologies are a challenge to execute for a

simultaneous oxygen evolution reaction (OER) along with H_2 generation. In addition, electron scavengers, such as $AgNO_3$, were also used to support the OER analysis without disturbing hydrogen production[92]. Thus, spinel materials with different nanostructures and morphologies have potential for photocatalytic hydrogen production, PEC water splitting and other applications.

4.2 Photocatalytic CO_2 reduction of spinels

The emission of carbon dioxide (CO_2) is a major contributor to global climate change. In order to solve this issue, carbon dioxide reduction can be achieved by numerous ways, such as biological reduction by plants, and thermal, electrochemical, or photocatalytic reduction. Among them, photocatalytic CO_2 reduction is a potential approach to convert CO_2 into useful products such as carbon monoxide (CO), methane, ethane, methanol, formic acid, formaldehyde, and etc[93-95] as shown in **Fig 5**. The photocatalytic reduction of CO_2 into hydrocarbon fuels is a promising method to recycle CO_2 as a fuel feedstock using solar energy, which is abundant, inexpensive, environmentally benign and safe. In order to develop highly efficient and active photocatalysts for CO_2 reduction to hydrocarbon fuels, such as dye degradation, H_2 generation and PEC water splitting, some essential conditions are (i) a narrow band gap to increase visible light absorption[96-98], (ii) proficient charge separation[99], (iii) a shift in the conduction band (CB) to a more negative region than the standard CO_2 reduction potentials[68]. Moreover, these photocatalysts should be stable, cost effective and eco-friendly. In this aspect, Wang et al.[100] prepared porous $ZnCo_2O_4$ nanorods as a co-catalyst for photocatalyst to convert CO_2 and water into H_2 and CO fuels. Besides, Limei et al.[101] prepared $CoAl_2O_4$, $MgFe_2O_4$ and $CoFe_2O_4$ spinel nanoparticles by an inorganic salt sol-gel method and annealed at 800 °C for 4 h for application of producing formic acid via photocatalytic reduction of CO_2. All three samples exhibited narrow band gaps, i.e. $E_g < 1.55$ eV. During photocatalytic CO_2 reduction, $Na_2C_2O_4$ was used as the

electron donor. For the $CoFe_2O_4$ spinels, ~ 4988.11 μmol h^{-1} g^{-1} of formic acid was produced at 5 h light irradiation time. It was shown that $CoAl_2O_4$, $MgFe_2O_4$ and $CoFe_2O_4$ spinel photocatalysts all possess high activity; where $CoFe_2O_4$ (~ 4988.11 μmol h^{-1} g^{-1}) was the best when compared to $CoAl_2O_4$ (~ 3950 μmol h^{-1} g^{-1}) and $MgFe_2O_4$ (~ 3100 μmol h^{-1} g^{-1}). The enhanced activity was attributed to the narrow band gap and the reductant $Na_2C_2O_4$. The reductant of $Na_2C_2O_4$ has a low redox potential, and can promote oxidation of the three spinel catalysts in the valence band holes. Moreover, the addition of $Na_2C_2O_4$ in the photocatalytic system not only offers more carbon sources, but also promotes CO_2 photoreduction to produce formic acid.

Recently, spinels of $CdIn_2S_4$ micro spherical structures were prepared by hydrothermal method[102] using three different sulfur precursors, such as L-cysteine and thioacetamide and thiourea. The samples were used to reduce CO_2 via photoactivity to valuable chemicals of dimethoxymethane (DMM) and methyl formate (MF). Notably, the catalyst prepared from L-cysteine revealed a unique photocatalytic activity in both chemical products of DMM (~ 2968 μmol h^{-1} g^{-1}) and MF (~ 2857 μmol h^{-1} g^{-1}). However the other two catalysts fabricated by thioacetamide and thiourea only stimulated the generation of MF, and the total chemical product formation rates were lower than $CdIn_2S_4$ produced from L-cysteine. To date, a large number of spinel photocatalysts including $ZnFe_2O_4$[103], $NiCo_2O_4$[104], $ZnCo_2O_4$[100], $MnCo_2O_4$[105], $CuCo_2O_4$[106], Co_3O_4[107], etc., have been used as a co-catalyst to enhance photocatalytic CO_2 reduction. However, there are only a limited number of reports on the use of pristine spinel material as an active catalyst in photoredox CO_2 conversion reactions.

4.3 Photoelectrochemical water splitting of spinels

Ferrites often exhibit excellent chemical and thermal stability in aqueous

environments[108]. The desired properties for semiconductors employed as electrodes in photoelectrochemical water splitting cells and/or as a photocatalyst include a narrow energy gap near ~ 2 eV. Most of the spinel ferrites are semiconductors with a narrow energy gap, that allow the absorption of a large part of the incident visible solar spectrum, and the energy gap permit excitation by visible light, and robust locations of the conduction and the valence bands favor both reduction of protons and/or oxidation of water. Many ferrites of the type MFe_2O_4[108] fulfill these important conditions since PECs containing photocathodes and/or photoanodes for water splitting with or without a small external bias in a three electrode PEC setup, where commonly for OER activity the alkaline environment is favored and for the hydrogen evolution reaction (HER) activity an acidic environment is favored.

Yang et al.[109] tested the photoelectrochemical performance of porous $CoFe_2O_4$ nanosheets on a fluorine-doped tin oxide (FTO) substrate. The electrodes were prepared from an aqueous solution of Co and Fe nitrate via a template-free electrochemical deposition, followed by heat treatment at 933 K. In a 0.1 M aqueous Na_2S solution at a zero bias voltage, the photoelectrode exhibited a small cathodic photocurrent of ~ 0.3 μA cm^{-2} under illumination by visible light ($\lambda \geq 390$nm, 30 $mWcm^{-2}$). Similarly, both amorphous and crystalline photocatalysts of mesoporous $NiFe_2O_4$ spheres were prepared by Hong et al.[110] using aerosol spray pyrolysis, where Pluronic F127 was used as the structural directing agent. It was found that the final structure of $NiFe_2O_4$ depends on the amount of the structure-directing agent and calcination temperature. The photocatalytic activity for hydrogen evolution was measured in methanol/water under 450 nm visible light illuminations. A long-term stability with high H_2 gas production of ~ 0.09 μmol h^{-1} was obtained for crystalline $NiFe_2O_4$, which was mainly due to the high crystalline nature of the nickel ferrites rather than large surface area.

It has recently been discerned[111] that photocatalytic water splitting can be a novel, green and economic way for water decomposition with a high solar-to-hydrogen conversion (SHF) efficiency. However, this SHF has yet to achieve efficiency above 46%. $NiFe_2O_4$ is one of the few materials where photocatalytic hydrogen production under irradiation by visible light in the absence of sacrificial reagents that have been reported[111]. Also, the enhanced electrical conductivity associated with the corresponding bare and/or pristine metal oxide (iron oxides; cobalt oxides, aluminum oxides etc.,) is due to the presence of different metal cations assisting the electron transport process and/or supporting the redox reactions at the electrolyte - semiconductor interface; this has a major significance in designing high performance water spitting systems and there are limited reports on PEC water splitting[108, 112, 113].

Tahir et al.[113] reported the photo anodic behavior of the n-$ZnFe_2O_4$ photoelectrode. The electrode was prepared by aerosol-assisted chemical vapor deposition using different alcoholic solutions of a bimetallic precursor on an FTO substrate. The photoanode thin film thickness, surface morphology, and nanostructures were controlled during fabrication. It was found that, nanocrystalline $ZnFe_2O_4$ showed an n-type nature, and the photoelectrode exhibited a maximum current density of ~350 μA cm^{-2} at 0.44 V *vs*. Ag/AgCl. This electrode was prepared at 450 °C with a deposition time of 35 min, where the precursors were prepared using an ethanol solution. It was revealed that the PEC performance of this $ZnFe_2O_4$ photoelectrode was dependent on the precursor solvent, deposition time and temperature. As a consequence, the photoelectrode showed an incident photon to electron conversion efficiency (IPCE) of ~ 13.5% at 0.23 V *vs*. Ag/AgCl in 3 M KCl at 350 nm wavelength light irradiation.

A pure orthorhombic crystalline phase of $MgFe_2O_4$ exhibits a band gap of ~ 1.91 eV for visible light absorption[108, 112]. The photoelectrochemical water splitting of $MgFe_2O_4$ was

examined by using photocurrent–potential curves in 1 M NaOH electrolyte under AM 1.5 mW cm^{-2} illumination. At 0.5 V *vs*. Ag/AgCl, the $MgFe_2O_4$ photoelectrode exhibited a photocurrent density of ~ 25 μA cm^{-2}. The PEC analysis of mixed phase of $Co_{3-x}M_xO_4$ [where M = (Al, Ga, In)] thin films were investigated as a function of Al : Ga by Newhouse et al.[67] Thin films of equal thickness were prepared by an inkjet method and during their PEC experiment, 0.1 M NaOH was used as an electrolyte. The optimized $Co_{3-x}M_xO_4$ film with x = 0.4 (i.e. M= Al: Ga: in ratios of ~1.5: 1: 1.9 at x = 0.4) showed an enriched cathodic photocurrent as the potential was swept from a negative to ~ -0.1 V, and showed a maximum current density of -0.1 mA cm^{-2} at -0.4 V *vs*. Ag/AgCl and exhibited diode features compared to the pristine Co_3O_4 film which displayed a substantial dark current. The high dark current could be due to the compensation of native defects in Co_3O_4 and low resistance of this material. This work validated the effect of band gap engineering in water splitting.

Recently cubic structured spinel chalcogenides have been used as photoelectrode materials for water splitting. Since the general formula of a normal 1-3 spinel is $M_{1/2}^{+}\,M_{1/2}^{3+}\,(M_2)^{3+}\,X_4^{2+}$ where the cations in the brackets occupy octahedral sites and the residual cations fill tetrahedral sites[114, 115]. Herein, the cubic spinel of $CuIn_5S_8$ is an n-type semiconductor and $CuIn_5S_8$ may be written as $Cu_{1/2}In_{1/2}(In_2)S_4$. This formulation can also be comprehended by replacing monovalent copper cations and trivalent indium cations for divalent cadmium cations in $CdIn_2S_4$, which is, however, a partial inverse thiospinel: $Cd_{1/2}In_{1/2}(Cd_{1/2}In_{3/2})S_4$. The photoelectrochemical behavior of n-type $CuIn_5S_8$ has been studied in various electrolytes. Scrosati and Fornarini[116] reported the impact of forbidden band gap of $CuIn_5S_8$ photocatalysts on the performance for PEC water splitting. The forbidden band gap of $CuIn_5S_8$ was found to be ~ 1.26 eV, which was nearer to the optimal value for solar energy utilization than its structural analogue $CdIn_2S_4$ (2.28 eV). The $CuIn_5S_8$ photoanode was more stable in the sulfide- polysulfide

electrolyte. The $CuIn_5S_8$ showed a negative value for the flatband potential, of ~ -1.2V *vs*. saturated calomel electrode (SCE) with a solar conversion efficiency of ~ 0.4%. The most negative values have been observed in the sulfide-polysulfide solution, which was due to specific adsorption of S^{2-} ions on the surface of electrode.

Moreover, amorphous spinel of $CdCr_2S_4$ photoelectrode was prepared using an indium tin oxides (ITO) glass as the substrate though a chemical bath deposition method[117]. The photoelectrochemical measurements were made at room temperature in 0.1 M polysulphide solution. Under light illumination, the electrode offered ~ 5.5 mA cm^{-2} at -0.1 V *vs*. SCE. This performance was attributed to the film being composed of small elongated particles of length of ~ 100-150 nm and diameter of ~ 10–20 nm and they were aggregated into monodispersed 100-400 nm diameter spherical clusters. Moreover, numerous nano-sized photoelectrode materials based on Co_3O_4 spinels have been developed for PEC water splitting. Recently, large scale production of spinels of $NiCo_2O_4$ with an urchin-like nanostructure by a simple hydrothermal method was reported[118]. Pristine urchins of $NiCo_2O_4$ with a diameter of 5 μm on which several small sized nanorods of $NiCo_2O_4$ with diameters of 100–200 nm and a length of 2 μm were radially grown from the center. The $NiCo_2O_4$ with an urchin-like nanostructure showed a high surface area of ~ 99.3 m^2 g^{-1}. As a result, a high photocurrent of ~ 70 μA cm^{-2} with excellent stability was observed for this urchin-like nanostructured $NiCo_2O_4$/FTO substrate. This enhanced performance was due to the large surface area, structural features and conductive nature of the sample.

It is of interest to study the photoelectrochemical properties of spinels for water splitting applications. Aviles et al. [119] reported that the fundamental band gap for Zn_2SnO_4 is about ~ 3.6−3.7 eV with a direct-forbidden transition. The conduction band position was predictable from the flat band potential (E_{fb}) using the photocurrent onset potential. In aqueous and non-

aqueous mediums the flat band potential of n-Zn_2SnO_4 was found to be more positive than anatase by electrochemical analysis. In addition, in aqueous solutions the E_{fb} of Zn_2SnO_4 was found to follow a ~ 59 mV/pH slope with E_{fb} extrapolated at pH = 0 of 0.08 V *vs*. normal hydrogen electrode (NHE). Under light illumination, the Zn_2SnO_4 exhibited an excellent photocurrent density of ~ 7 mA cm^{-2} V *vs*. NHE.

Photoelectrochemical water splitting by spinels under visible light remains the utmost desirable hydrogen and/or oxygen production method for fossil fuel energy. Chemical stability, light absorbing capability and low resistive spinel materials with aligned band edges to the water redox potentials have been the major focus for material scientists, but no solution has been revealed. Although tunable band gaps in the visible range were obtained, the material performance was restricted by reduced carrier transport properties connected with small polaron carriers[120]. A systematic understanding of the foremost material factors restraining their performance is presently lacking. In order to disclose this, spinels of $CuFe_2O_4$, $MgFe_2O_4$ and $ZnFe_2O_4$ were prepared by a solution-based approach[121] and their photoelectrochemical (PEC) water splitting activity was assessed, as shown in **Fig. 6**. Annealing post-treatments together with the deposition of $NiFeO_x$ over-layers were found to enhance the native n-type response, although dominant bulk charge recombination, especially in $MgFe_2O_4$ confine the saturation photocurrent below ~ 0.4 mA cm^{-2} at 1.23 V *vs*. reversible hydrogen electrode (RHE). In addition, extended Fermi level pinning was observed, which was due to surface states at around 0.9 V *vs*. RHE. The $NiFeO_x$ overlayer was ineffective in modifying the pinning of the Fermi level, but evidently participated as an electrocatalyst to improve the overall activity.

5. Ways to enhance the overall photocatalytic performance

As shown in **Table 1,** the spinel photocatalysts are surveyed on the basis of their performance in environmental remediation, hydrogen generation, CO_2 reduction and photoelectrochemical water splitting through an overall perspective. However, the long term operational stability and efficiency are often compromised of these strategies, restricting the large-scale application of spinel photocatalysts. Hence, a desired amount of dopant species, hetrostructure formation, enhancement in surface area with highly porous nature and high crystalline natures were introduced by the scientific community in order to improve their applicability in practice as shown **Fig. 7**.

5.1 Selective doping on spinels

Substituting a small fraction of the cations/anions of a "host spinels" is an effective method to improve the performance of spinels[122-125]. Typically, a suitable dopant can act as an efficient scavenger to trap electrons, and hence significantly prevent the recombination of photoinduced electron-hole pairs, whereas subsequently the photocatalytic activity as well as photosensitivity will be enhanced tremendously. Besides, doping of spinel photocatalysts by an appropriate dopant can modify the surface structure, enhance spectral response and also regulate the electrocatalytic active sites[126]. Moreover, in some cases the doping could potentially reduce the band gap. Also, the active centers in such an arrangement could be either the oxygen particles nearby the dopant, or the dopant itself. Recently, several research groups[17, 127, 128] have prepared the spinel oxides either with the formula AB_2X_4, and/or $(B(AB)O_4)$, which combine two (or more) different metal ions. However, only limited research studies[129-132] have examined ternary transition metal oxides with a spinel oxide structure and their site-preferences, despite reports[133] of enhanced activities for the photocatalytic performance. Mg doped $CoFe_2O_4$ was proposed as a photocatalyst to degrade RhB by Sundararajan et al[134]. The maximum photocatalytic degradation efficiency of 99.5 %

was observed for 0.4 wt% Mg doped $CoFe_2O_4$ (i.e. $Co_{0.6}Mg_{0.4}Fe_2O_4$ sample), which was ~ 1.37 times higher than the pristine $CoFe_2O_4$ (~ 73.0%), i.e. after Mg doping the degradation efficiency was enhanced by about ~ 26.5%. This was mainly due to the effective charge separation and prevention of electron-hole pair recombination. The photo induced electron-hole pair recombination might be depressed due to the increase in band gap value with an addition of Mg and thus it was accessible for the charge carriers to endure effective RhB dye degradation. Likewise, various dopants with spinels were used for photocatalytic degradation to enhance the performance. Cobalt mixed-metal spinel oxides, $Co(Al_{1-x}Ga_x)_2O_4$, are promising as photocatalysts for photodegradation of methyl orange and phenol[135], as shown in **Fig. 8**. This study showed that the dye degradation activity of $Co(Al_{0.5}Ga_{0.5})_2O_4$ was dependent on both pH and the substrate. For $Co(Al_{0.5}Ga_{0.5})_2O_4$, an efficiency of 46% and 72% was observed for photodegradation of methyl orange and phenol respectively. Also, spinel $ZnFe_{2-x}Cr_xO_4$ nanoparticles was used to remove orange I azo dye from an aqueous solution[136].

Anion doping is also effective in enhancing the photocatalytic performance. Lin et al.[137] prepared sulfur anion doped Zn_2SnO_4 for RhB dye degradation under visible light. The doping of anion of S^{2-}significantly reduced the band gap to 2.7 eV, comparing to that the band gap of pristine Zn_2SnO_4 was ~ 3.6 eV. Owing to the band gap shrinkage the sulfur doped Zn_2SnO_4 revealed an excellent photodegradation of RhB in aqueous solution under visible light irradiation. Similarly, taking advantage of the effect of anion (Fluorine) doping, Huang et al.[138] attained ~ 2.6 times enhanced photocatalytic RhB dye degradation activity for fluorine doped $ZnWO_4$ (F-$ZnWO_4$) than the pristine $ZnWO_4$.Recently, nitrogen-doped carbon@$NiCo_2O_4$ (NC@$NiCo_2O_4$) was prepared by Wang et al[139]. for the visible light photocatalytic reduction of CO_2. This structural and functional property of catalytically active Co and Ni with conductive nitrogen-doped carbon showed a remarkable separation of photogenerated charge carriers, which

enhanced the adsorption and concentration of CO_2 molecules and also offered more active sites for photocatalytic reactions. These exceptional structural and compositional features greatly enhanced the performance for the deoxygenative reduction of CO_2, of about ~ 26.2 μmol h^{-1} with a high CO evolving rate of ~ 2.62×10^4 μmol h^{-1} g^{-1} and good stability.

In order to enhance water splitting efficiency, Xu et al.[140] prepared $ZnFe_2O_4$, $ZnFeGaO_4$ and $ZnGa_2O_4$ spinels[140]. Among them, $ZnFeGaO_4$ showed considerable absorption in visible light, with an energy gap of ~1.9 eV. This spinel showed an improved hydrogen production rate of ~ 971 μmol $h^{-1}g^{-1}$ compared to pristine $ZnFe_2O_4$, i.e. ~861 μmol h^{-1} g^{-1} under a whole solar spectrum. Doping of Ga into the $ZnFe_2O_4$ spinel structure enhanced the UV region light absorption and altered the electronic configuration, which enhanced the photocatalytic activity. An investigation found that the optical properties were subjected to d → d transitions caused by d orbitals of Co(II) split into Co e_d and t_{2d} states under the tetrahedral crystal field (i.e. A site in AB_2O_4 spinel structure)[120]. In addition, the doping of Ga and In for Al at the B site was observed to reduce the energy gap through both enriched O 2p–Ga/In d coupling and an increased influence of group 13 cations states; moving the conduction band downward. While tunable band gaps in the visible range can be obtained, the material performance was limited by poor carrier transport properties associated with small polaron carriers. Similarly, it was designed that the electronic structure of these cobalt based metal spinel oxides could be further tuned by establishing cobalt mixed-metal spinel oxides $Co(Al_xGa_yIn_{1-x-y})_2O_4$ to shrink the energy gap and increase orbital mixing, which could lead to enhanced charge carrier mobility[141].

Likewise, Woodhouse et al.[142, 143] prepared p-type $Co_{3-x-y}Al_xFe_yO_4$ spinel oxides with tunable band gaps from ~ 1.6 to 2.0 eV by changing the Fe:Al ratio. This photoelectrode material showed weak cathodic photocurrent under a negative bias. The poor PEC activity was later ascribed to the

poor electrical conductivity. Similarly, Miao et al[144]. testified the $ZnFe_2O_4/Fe_2O_3$ composite as the photoanode for PEC water splitting, and after doping hematite with Ti, a photocurrent up to ~ 0.15 mA cm^{-2} was obtained.

5.2 Heterojunction on spinels

It is well known that, photocatalytic or PEC system is a simplistic method for the conversion and utilization of solar energy. To date, several semiconducting spinel photocatalysts have been developed for the aforementioned photocatalytic reactions. Nevertheless, photocatalyst of inorganic materials has certain disadvantages, such as limited concentration of exposed active sites and poor stability. Hence, the development of efficient photocatalytic materials by forming the heterojunction has attracted enormous research interests. Also, the strategy of a heterojunction formation is an effective way to improve the photocatalytic activity, due to the rapid separation of charge carriers made by the built-in electric field. Moreover, combination of proper spinel semiconductors can also render improved photostability and photoabsorption[145, 146]. Recently, Nguyen et al.[66] reported the photocatalytic degradation of Bisphenol A (BPA) using visible-light-sensitive $ZnFe_2O_4$–TiO_2 heterojunction photocatalysts. At a 465 nm light irradiation condition, the reaction rate of BPA by $ZnFe_2O_4$–TiO_2 was 42 times greater than that under 365 nm UV light irradiation, as shown in **Fig. 9**. The $ZnFe_2O_4$–TiO_2 nanocomposites displayed outstanding recycling and reusability and it could retain a stable photocatalytic performance for at least 10 reaction cycles, with a rate constant of ~ 0.191-0.218 min^{-1} under visible light irradiation during photodegradation of BPA. Later, Hamad et al.[147] fabricated TiO_2–SiO_2–$CoFe_2O_4$ core–shells by a sol-gel/hydrothermal route, in which the middle layer SiO_2 acts as an insulator among the $CoFe_2O_4$ core and the TiO_2 shell, and facilitate the separation of the core and shell during photocatalysis reaction. The TiO_2–SiO_2–$CoFe_2O_4$ composite has been tested for degradation of dichlorophenol-indophenol (DCPIP) dye. During the dye

degradation reaction, the highest performance of ~ 95.32 and ~87.27% was attained for core-shell structure under UV and visible light respectively. Similarly, N-doped $TiO_2/ZnFe_2O_4$ showed an enhanced performance compared with $TiO_2/ZnFe_2O_4$ or $ZnFe_2O_4$ due to the construction of a heterostructure at the interface as well as the introduction of N species[148].

$NiFe_2O_4@TiO_2$ core-shell heterojunction was prepared by Kim et al[149]. Owing to the synergetic feature between the heterojunction of $NiFe_2O_4$ and TiO_2, it revealed the effective charge transfer from TiO_2 to $NiFe_2O_4$ and the suppression of electron/hole pair recombination significantly enhanced the photocatalytic activity. As a result, H_2 production from the photo-splitting of core-shell $NiFe_2O_4@TiO_2$ catalyst was ~ 10 times higher than either pristine TiO_2 or $NiFe_2O_4$. Moreover, core–shell photocatalysts of $Fe_3O_4@ZnS$ and $NiCoO_4@ZnS$ was prepared and used for photocatalytic H_2 production[135]. It was observed that, the performance of H_2 production can be tuned by the alteration of electronic structure and morphology of the core-shell materials. By adding different concentrations of ZnS into $CoFe_2O_4$, the $CoFe_2O_4@ZnS$ core-shell photocatalyst was prepared by Chang et al[150]. They perceived an improved H_2 production rate of 1650 μmol g^{-1} h^{-1} for $CoFe_2O_4@ZnS$ photocatalyst calcined at 500 °C. This enhanced photocatalytic activity was accredited to the development of a heterojunction at the interface. Moreover, the formation of heterojunction using the organic materials hold several benefits, such as low cost, easy fabrication, and good flexibility. In order to photocatalytic degrade MB dye, the spinel of $NiFe_2O_4/g\text{-}C_3N_4$ was made by Liu et al[151]. Owing to the higher catalytic active sites, the 2 wt. % of $NiFe_2O_4/g\text{-}C_3N_4$ photocatalysts showed an excellent degradation activity than pristine $NiFe_2O_4$. Besides, $CoFe_2O_4/g\text{-}C_3N_4$[152] and $Au/g\text{-}C_3N_4/NiFe_2O_4$[153] photocatalysts have also showed enhanced photocatalytic activities. In conclusion, as shown in **Fig. 10,** the enhanced activity was attributed to the heterojunction on photocatalysts that can accelerate the separation of electron-hole pairs and also increase the fascinating optical property.

Additionally, the spinel of $ZnFe_2O_4$ is stable in both acidic and alkaline environments[154], and the conduction band (CB) and valence band (VB) edge positions of $ZnFe_2O_4$ are more negative which favor the PEC water splitting application[154]. Therefore, heterojunction structure of $ZnFe_2O_4$ with Fe_2O_3 and Ti can improve the electron-hole pair separation more efficiently than α-Fe_2O_3 and Ti. In this aspect Fe_2O_3:Ti/$ZnFe_2O_4$ heterojunction photoanodes were prepared by Miao et al[144]. As a result, the Fe_2O_3:Ti/$ZnFe_2O_4$ photoanode revealed the high photocurrent of ~ 0.27 mA cm^{-2} at 1.23 V *vs*. RHE. Later, Luo et al[155]. reported a highly oriented nanocolumnar heterojunction structure of α-Fe_2O_3/$ZnFe_2O_4$ by the atomic layer deposition technique. Owing to the heterojunction feature, the maximum photocurrent density of ~ 0.8 mA cm^{-2} at 1.23 V *vs*. RHE was attained. In addition, Liu et al[156]. prepared a nanorod array of α-Fe_2O_3 covered $ZnFe_2O_4$, which resulted in the formation of $ZnFe_2O_4$/α-Fe_2O_3 heterojunctions with a superior current density of ~ 0.29 mA/cm^2 at 1.23 V *vs*. RHE. These outcomes demonstrate that, the heterojunction engineering can effectively promote the charge separation, expose more active sites, increase the conductivity and thereby enhance the photocurrent density.

Developing efficient photocatalysts for solar-driven CO_2 reduction is appropriate to improve CO_2 photoreduction performance for real-world application. Due to their distinct physicochemical features, heterostructured spinels are excellent photocatalysts for CO_2 conversion[157, 158]. To date, several spinel structures have been used to maximize the virtues of heterojunction for photocatalysis with proper nanostructures[159]. In this aspect, very recently, Wang et al.[132] prepared hierarchical tubular heterostructured $ZnIn_2S_4$–In_2O_3 by a hydrothermal method as shown in **Fig**. **11.** This special structural features exposed more active sites, facilitated the facile transfer of photogenerated charge carries and large surface area. As a result, the $ZnIn_2S_4$-In_2O_3 photocatalyst showed exceptional performance for deoxygenative CO_2 reduction with significant CO evolution rate of ~ 3075 μmol h^{-1} g^{-1} and long term

stability. Similarly, various kinds of heterostructured spinels such as $ZnFe_2O_4$-BiOCl[160], Co_3O_4–CeO_2[161] and $ZnFe_2O_4/TiO_2$[162] were tested for photocatalytic CO_2 reduction reaction.

5.3 Porosity and surface area

The surface area and porosity also strongly influence the photocatalytic activity, as the porous structure is beneficial for the absorption and diffusion of target molecules into the active sites. The electron–hole recombination might also depend on the porosity and size of the nanoparticles. In addition, a higher surface area might increase the light absorption and carrier collection and hence enhance the performance for PEC water splitting. Typically, common synthesis methods such as hydrothermal, solvothermal, co-precipitation, chemical etching, electrospinning (including sol-gel), and templating synthesis have been widely used to improve the porous nature with large surface areas of spinels. Benefitting from the porous nature, numerous research groups have achieved outstanding performances in photocatalytic systems.

5.3.1 Hydrothermal and Solvothermal synthesis

Hydrothermal and solvothermal synthesis are crystallization processes in high-temperature solutions (aqueous or organic solvents) at high vapor pressures, which are the most widely used methods for preparing metal oxides. Dhiman et al.[72] prepared $ZnFe_2O_4$ with different morphologies i.e. porous nanorods, nanoparticles, nanoflowers and hollow microspheres using the hydrothermal method. The application of synthesized $ZnFe_2O_4$ nanostructures was studied in photo-Fenton degradation of dyes. The results indicated shape dependent relationship with photocatalytic activity as the degradation of dyes followed the order porous nanorods > nanoparticles > nanoflowers >hollow microspheres. Also, Liu et al.[163] synthesized two-dimensional porous Co_3O_4 sheets through a hydrothermal route, which exhibited higher performance for photocatalytic degradation of methylene blue (MB) than the

bulk Co_3O_4. Foletto et al.[164] synthesized $ZnAl_2O_4$ nanoparticles by co-precipitation, hydrothermal and microwave-hydrothermal methods and studied the effects of preparation method on the pore size and photocatalytic efficiency. It was found that the pore size influences the catalytic performance significantly. The sample prepared by co-precipitation showed the highest activity due to its largest pore size. Similarly, Anchieta et al.[165] prepared Zn_2SnO_4, $ZnAl_2O_4$ and $ZnFe_2O_4$ powders with large surface areas by hydrothermal, metal–chitosan complexation and solvothermal routes, respectively, in which Zn_2SnO_4 showed the highest performance for photodegradation of phenol.

Porosity and surface area also influence the performance of other photocatalytic process significantly. For example, three dimensional (3D) hierarchical cobalt ferrite/graphene aerogels ($CoFe_2O_4$/GAs) composites were prepared by a hydrothermal process[166]. The $CoFe_2O_4$/GAs composites revealed 3D hierarchical pore structure with mesopores about 14~18 nm, macropores of 50~125 nm, and a remarkable surface area of ~ 177.8 $m^2 g^{-1}$. These functionalities provided this hybrid composite with high biodegradable Photo-Fenton activity for methyl orange dye pollutant degradation. Further, the $CoFe_2O_4$/GAs could also operate in a wide pH range. When compared with the mechanically mixed composites of $CoFe_2O_4$/reduced graphene oxide ($CoFe_2O_4$/RGO), the $CoFe_2O_4$/GAs composites exhibited an interconnected 3D porous structure with uniform deposition of $CoFe_2O_4$ nanoparticles, as shown in **Fig. 12**, which may capture electrons to ease the Fe^{3+}/Fe^{2+} conversion in Photo-Fenton reaction. Thus, the $CoFe_2O_4$/GAs hybrid composites showed an excellent degradation of methyl orange dye pollutant. The porous 3D structure provided short diffusion pathways, admirable conductive network and large surface area, which is also beneficial for the Photo-Fenton reactions. Furthermore, mesoporous ultrathin $ZnGa_2O_4$ photocatalyst was prepared by a facile solvothermal route[167]. Inheriting both a high

crystalline nature and high surface area (110.4 m^2 g^{-1}) afford by mesoporous nanosheets of the unique 3D hierarchical nanostructures revealed a great CO_2 photocatalytic performance. Besides, benefiting from the meso-$ZnGa_2O_4$ porous nature, the photo-excited carriers can persist longer period on the nanosheet, which also contributed to the high photocatalytic activity of the $ZnGa_2O_4$ nanosheets.

5.3.2 Chemical etching method

Chemical etching allows the selective removal of less stable regions in a bulk material, giving rise to porous structures. It has been extensively used for preparing porous materials such as activated carbons. Very recently, Yao et al[168] prepared the highly activated porous carbon and its hybrid of $Fe_3C/Fe_3O_4/C$ nanosheets via etching using HCl. As a consequence of its high porosity, large surface area and highly active nature, this hybrid revealed an excellent photocatalytic activity. Also, Pang et al.[169] prepared porous $ZnFe_2O_4$ by etching $ZnFe_2O_4$ particles with oxalic acid, and the porosity was controlled by changing the etching time. As expected, they found that $ZnFe_2O_4$ particles with higher porosity and specific surface area exhibited a higher efficiency towards photocatalytic degradation of RhB. Similarly, benefiting from the etching technique, the enhanced photocatalytic performances were attained for carbon dots/$NiCo_2O_4$ composite[170], N-doped carbon@ $NiCo_2O_4$[139], Co_3O_4[171] and $NiCo_2O_4$[171] etc.

5.3.3 Electrospinning

Electrospinning works through stretching of a polymer solution (or melt) to an enormous draw ratio using electrical force. It is a versatile technique to prepare one-dimensional nanostructures. Metal oxides prepared through such a process might possess large surface areas and high porosity after removal of the polymer matrix upon calcination. Porous spinel nanotubes and nanofibers have been prepared by this method. For instance, Jing et al[172, 173]. prepared porous

tetragonal-$CuFe_2O_4$ nanotubes by electrospinning. In such a process, the precursor was first prepared through a sol-gel process, followed by air-annealing during which the polymers were removed as gases and metal ions diffuse and pores were developed. The nanotubes displayed excellent performance for photodecomposition of acid fuchsin. Using a similar method[173], they prepared hierarchical $SrTiO_3/NiFe_2O_4$ composite nanotubes with excellent light response and high performance for degradation of RhB.

5.3.4 Template synthesis

Template synthesis involves the patterning and growth of building blocks of the target materials on the template which could be in the form of soft template, hard template or self-template. The formation of porous materials can be well controlled in this process, which usually results in ordered structures. Skliri et al[174]. prepared a 3D interconnected nanoporous $ZnFe_2O_4$ with a large internal surface area (up to 159 $m^2 g^{-1}$) through a block copolymer-assisted cross-linking aggregation of colloidal nanoparticles, which showed a photocatalytic rate of five times higher than the bulk counterpart towards reduction of aqueous Cr(VI). Zhang et al.[175] prepared $CuCr_2O_4$ mesoporous structure by casting mixed melt of $Cu(NO_3)_2$ and $Cr(NO_3)_3$ into cubic *Ia*3*d* mesoporous silica template KIT-6, followed by removing the template using KOH. It was shown the mesoporous $CuCr_2O_4$ exhibits significantly higher efficiency towards photoelectrocatalytic hydrogen production than the bulk counterpart. Furthermore, the stability under visible light was also enhanced in the porous structure than in the bulk material. Similarly, porous Co_3O_4 nanostructures have been prepared[176, 177] using polyvinyl pyrrolidone modified carbon spheres as the template, which exhibited higher performance than the bulk Co_3O_4 for photocatalytic degradation of Congo Red. $Ni_{1-x}Co_xFe_2O_4$ microcubes have also been prepared by pyrolysis of metal-organic framework at 600 °C with the assistance of sacrificial templates[178]. Hong et al.[110]

prepared mesoporous nickel ferrite ($NiFe_2O_4$) spheres by an aerosol spray pyrolysis method using Pluronic F127 as a structure-directing agent, as shown in **Fig. 13**. As a result, the high specific surface area (~ 278 m^2 g^{-1}) with a highly crystalline framework was attained by changing the quantity of structure-directing agent and the calcination condition. Also, spinel structured $CuCr_2O_4$ with mesoporous structure have been successfully synthesized using a nanocasting method[179]. Owing to the mesoporous nature, the spinel $CuCr_2O_4$ nanostructure found to be active for low temperature CO oxidation.

5.3.5 Direct pyrolysis

Pyrolysis is an essential step for synthesize of spinels in most of the preparation methods, during which the precursor plays an important role in the morphology of the final products. Meng et al[180]. prepared highly porous $ZnFe_2O_4$ through pyrolysis of zinc-iron(III)-sulfate layered double hydroxide (LDH). They also prepared $ZnFe_2O_4$ by a conventional co-precipitation route followed by calcination under the same conditions for comparison. It was found the sample prepared by the former method exhibits higher efficiency and longer lifetime for catalytic degradation of phenol than that of the latter. Liu et al[181]. prepared $MnFe_2O_4$ by co-pyrolysis of $Mn(NO_3)_2$, $Fe(NO_3)_3$ and rice hull. The complexation of metal ions with the polar group in rice hull and the carbonization of the latter gave rise to highly porous $MnFe_2O_4$. Furthermore, porous $CoFe_2O_4$ was also prepared through similar procedures, which showed excellent performance for degradation of methylene blue. Direct pyrolysis of carbonate precursors also resulted in highly porous $CoMn_2O_4$ and $MnCo_2O_4$ catalysts with high performances[182]. The different porosity and surface areas derived from different precursors might be associated with the different thermal stability and ease of gasification of the precursor. The different morphologies of the precursors might also play a role as it can be inherited into the pyrolytic product.

5.4 Nano size crystalline effect

The crystalline size is also a crucial factor that determines the photocatalytic performance. The reduced crystalline size would provide shorter diffusion length of photogenerated carriers during the photocatalytic reactions, which could enhance the photocatalytic activity. Usually, an increase in particle size was observed in spinels annealed at higher temperatures due to a blending of neighboring particles. In some cases, their crystallinity is also increased[183]. The annealing effect of $ZnFe_2O_4$ for photodegradation of methyl orange was reported by Jadhav et al[184]. The $ZnFe_2O_4$ sintered at 500 °C showed the best methyl orange photodegradation activity, which was ascribed to a regular crystallization of zinc ferrite at this temperature. A further increase in the heat treatment temperature led to a decrease in performance, which was due to the increased bulk crystalline nature of the samples. Likely, ferrites of MFe_2O_4 (M = Co, Ni, Zn, Cu) were prepared by Sharma et al.[71] and their results indicate that the samples annealed at 400 °C had a higher efficiency when compared to the samples annealed at 1000 °C and also perceived high photodegradation activity. Moreover, one dimensional $ZnFe_2O_4$ nanorods with a diameter of ~ 40 nm and length of ~ 400 nm were prepared on an FTO glass substrate by Kim et al[185]. In order to enhance the crystalline nature and PEC performance, the prepared samples were used for normal thermal treatment and hybrid microwave annealing (HMA) from 550 to 800 °C for 3 h. As a result, the 550 °C-annealed $ZnFe_2O_4$ photoanode showed an excellent PEC activity, which was ~15 times higher than the 800 °C-annealed one (i.e. a conventionally annealed $ZnFe_2O_4$ sample). It was observed that hybrid microwave annealing enhanced the crystallinity of $ZnFe_2O_4$ nanorods compared to conventional annealing. In addition, these experiments revealed that an improved hole injection for water splitting was probably due to reduced surface trap sites and increased crystallization of the bulk $ZnFe_2O_4$ spinel.

It should be pointed out, however, the practical application of these spinel hetrostructures is still at an early step and has a prolonged way to go. As shown in **Table 1**, several spinel materials can act as effective photocatalysts for environmental remediation, hydrogen generation, CO_2 reduction reactions and PEC water splitting. Nevertheless, the photocatalytic performances for some of the above-mentioned spinels are still inferior to some of the non-spinel semiconductor photocatalysts such as TiO_2, ZnO, CdS and etc, not to mention that preparation of some of the conventional semiconducting catalysts are more straightforward. Compared to spinel photocatalysts, the band gaps and energy levels of some non-spinel photocatalysts are more appropriate for harvesting solar energy, which bring up excellent photocatalytic performances. However, as explained above, spinels as a rising catalyst platform could offer even richer space for tailoring of the composition, morphology, crystallite structure and performance which could be fulfilled by doping, heterojunction, pore-creating, crystallite shrinking and so on. In this sense, spinels would be promoting photocatalysts in future.

6. Conclusions

In summary, spinel materials are promising candidates for a wide range of applications including green and clean use of environmental remediation, photocatalytic hydrogen production, CO_2 reduction and photoelectrochemical water splitting. A number of spinels including those based on cobalt, copper, nickel, zinc, iron and several other mixed-metal oxide spinels have been designed for a variety of photocatalytic reactions. Ultimately, the spinel materials are cost effective, eco-friendly, highly stable and naturally abundant. However, the use of these spinels continues to develop, because of their relatively low efficiency towards generation of fuels, although the possibilities to exploit green methods for the production of fuels and chemicals while reducing the global CO_2 level makes it an fascinating material to be explored and

advanced. Notably, some spinels such as $ZnFe_2O_4$, $CoFe_2O_4$, $BaFe_2O_4$, $MnFe_2O_4$ and $MgFe_2O_4$ etc., exhibit a narrow band gap, photo-Fenton reaction, high porosity with large surface area, and fine nanostructure, which are beneficial for photocatalytic applications when exposed to the visible light spectrum. However, there remain potential challenges such as inadequate photoabsorption in the visible light region, poor efficiency, reduced chemical absorption and activation of CO_2 reduction, and low electron–hole charge separation efficiency. Nevertheless, spinel nanostructures have shown great opportunities in environmental remediation and hydrogen production. The applications of the spinels for the photoreduction of CO_2 are less widely reported and most spinels were used as a co-catalyst with high cost precious ruthenium compounds. Importantly, the spinel materials offer a substantial platform for structural, electronic and surface modification, doping with other transition metals or carbon materials. It is envisioned that these materials can fulfill their potential as a photocatalyst for dye degradation, CO_2 reduction, water splitting and applications in electronic and energy conversion, along with future storage devices such as, super capacitors, batteries, fuel cells and hybrid electric vehicles.

Acknowledgements

This work was supported by Shenzhen Government's Plan of Science and Technology (KQJSCX20170330110144O4), the National Natural Science Foundation of China (51602202, 21671136 and 51774203).

References

1. A. J. Bard, *Science*, 1980, **207**, 139-144.
2. A. Mills, R. H. Davies and D. Worsley, *Chem. Soc. Rev.*, 1993, **22**, 417-425.
3. A. B. Djurišić, Y. H. Leung and A. M. C. Ng, *Mater. Horizons.,* 2014, **1**, 400-410.
4. S. Shinde, C. Bhosale and K. Rajpure, *Catalyst. Rev.,* 2013, **55**, 79-133.

5. S. Chandrasekaran, E. J. Kim, J. S. Chung, I. K. Yoo, V. Senthilkumar, Y. S. Kim, C. R. Bowen, V. Adamaki and S. H. Hur, *Chem. Eng. J.,* 2017, **309**, 682-690.

6. S. Chandrasekaran, Y.-L. T. Ngo, L. Sui, E. J. Kim, D. K. Dang, J. S. Chung and S. H. Hur, *Dalton Trans.,* 2017, **46**, 13912-13919.

7. M. Ye, J. Gong, Y. Lai, C. Lin and Z. Lin, *J. Am. Chem. Soc,* 2012, **134**, 15720-15723.

8. M. Wang, J. Ioccozia, L. Sun, C. Lin and Z. Lin, *Energy Environ. Sci,* 2014, **7**, 2182-2202.

9. S. C. Markham, *J. Chem. Edu.,* 1955, **32**, 540.

10. A. Fujishima and K. Honda, *Nature*, 1972, **238**, 37.

11. S. J. Moniz, S. A. Shevlin, D. J. Martin, Z.-X. Guo and J. Tang, *Energy Environ. Sci,* 2015, **8**, 731-759.

12. M. Ge, C. Cao, J. Huang, S. Li, Z. Chen, K.-Q. Zhang, S. Al-Deyab and Y. Lai, *J. Mater. Chem. A, 2015,* 2016, **4**, 6772-6801.

13. M. Ge, Q. Li, C. Cao, J. Huang, S. Li, S. Zhang, Z. Chen, K. Zhang, S. S. Al□Deyab and Y. Lai, *Adv. Sci.* 2017, **4**.

14. M. Ge, J. Cai, J. Iocozzia, C. Cao, J. Huang, X. Zhang, J. Shen, S. Wang, S. Zhang and K. Q. Zhang, *Int. J. Hydrog. Energy*, 2017, **42**, 8418-8449.

15. S. Jauhar, J. Kaur, A. Goyal and S. Singhal, *RSC Advances,* 2016, **6**, 97694-97719.

16. K. Lee, D. A. Ruddy, G. Dukovic and N. R. Neale, *J. Mater. Chem. A,* 2015, **3**, 8115-8122.

17. E. Casbeer, V. K. Sharma and X.-Z. Li, *Sep. Purif. Technol.,* 2012, **87**, 1-14.

18. S. Chandrasekaran, J. S. Chung, E. J. Kim and S. H. Hur, *Chem. Eng. J.,* 2016, **290**, 465-476.

19. S. Chandrasekaran, E. J. Kim, J. S. Chung, C. R. Bowen, B. Rajagopalan, V. Adamaki, R. Misra and S. H. Hur, *J. Mater. Chem. A,* 2016, **4**, 13271-13279.

20. S. Chandrasekaran, J. S. Chung, E. J. Kim and S. H. Hur, *J Electrochem Sci Technol*, 2016, **7**, 1-12.

21. K. Jordan, A. Cazacu, G. Manai, S. Ceballos, S. Murphy and I. Shvets, *Phys. Rev. B,* 2006, **74**, 085416.

22. J. Tian, Z. Zhao, A. Kumar, R. I. Boughton and H. Liu, *Chem. Soc. Rev.,* 2014, **43**, 6920-6937.

23. J. Li and N. Wu, *Catal. Sci. Technol.* 2015, **5**, 1360-1384.

24. D. Liu, W. Zhu, J. Trottier, C. Gagnon, F. Barray, A. Guerfi, A. Mauger, H. Groult, C. Julien and J. Goodenough, *RSC Advances,* 2014, **4**, 154-167.

25. S. Zhu and D. Wang, *Adv. Energy Mater.* 2017, **7**, 1700841-1700865.

26. J. A. Byrne, P. S. M. Dunlop, J. W. J. Hamilton, P. Fernández-Ibáñez, I. Polo-López, P. K. Sharma and A. S. M. Vennard, *Molecules*, 2015, **20**, 5574-5615.

27. A. Kudo and Y. Miseki, *Chem. Soc. Rev.,* 2009, **38**, 253-278.

28. C. L. Muhich, B. D. Ehrhart, I. Al□Shankiti, B. J. Ward, C. B. Musgrave and A. W. Weimer, *WIRES: Energy. Environ.,* 2016, **5**, 261-287.

29. S. Dawood and T. K. Sen, *J. Chemi. Process. Eng.,* 2013, **1**, 1-7.

30. K. E. Sickafus, J. M. Wills and N. W. Grimes, *J. Am. Ceram. Soc.* 1999, **82**, 3279-3292.

31. S. Sun, H. Zeng, D. B. Robinson, S. Raoux, P. M. Rice, S. X. Wang and G. Li, *J. Am. Chem. Soc.* 2004, **126**, 273-279.

32. J. Gunjakar, A. More, K. Gurav and C. Lokhande, *Appl. Surf. Sci.*, 2008, **254**, 5844-5848.

33. Q. Zhao, Z. Yan, C. Chen and J. Chen, *Chem. Rev.,* 2017, **117**, 10121-10211.

34. M. A. Baqiya, A. Taufiq, K. Ayun, M. Zainuri and S. Pratapa, in *Magnetic Spinels-Synthesis, Properties and Applications*, InTech, 2017, 253-271..

35. P. A. Dickof, P. J. Schurer and A. H. Morrish, *Phy. Rev. B*, 1980, **22**, 115-127.

36. D. J. Singh, M. Gupta and R. Gupta, *Phy. Rev. B*, 2001, **63**, 205102.

37. H. Yahiro, H. Tanaka, Y. Yamamoto and T. Kawai, *Solid State Commun.,* 2002, **123**, 535-538.

38. S. A. Oliver, H. H. Hamdeh and J. C. Ho, *Phy. Rev. B*,, 1999, **60**, 3400-3405.

39. T. Shinagawa, M. Izaki, H. Inui, K. Murase and Y. Awakura, *Chem. Mater.*, 2006, **18**, 763-770.

40. S. Zhou, K. Potzger, D. Bürger, K. Kuepper, M. Helm, J. Fassbender and H. Schmidt, *Nucl. Instrum. Methods Phys. Res*, 2009, **267**, 1620-1622.

41. M. R. D. Khaki, M. S. Shafeeyan, A. A. A. Raman and W. M. A. W. Daud, *J. Mol. Liq.* 2017, **258**, 354-365.

42. D. Wang, T. Sheng, J. Chen, H. F. Wang and P. Hu, *Nat. Cat.*, 2018, **1**, 291-299.

43. S. Chandrasekaran, S. H. Hur, E. J. Kim, B. Rajagopalan, K. F. Babu, V. Senthilkumar, J. S. Chung, W. M. Choi and Y. S. Kim, *RSC Advances*, 2015, **5**, 29159-29166.

44. S. Chandrasekaran, S. H. Hur, W. M. Choi, J. S. Chung and E. J. Kim, *Mater. Lett.*, 2015, **160**, 92-95.

45. S. Battiston, C. Rigo, E. d. C. Severo, M. A. Mazutti, R. C. Kuhn, A. Gündel and E. L. Foletto, *Mater. Res.*, 2014, **17**, 734-738.

46. T. Tangcharoen, T. Jiraroj and C. Kongmark, *J. Mater. Sci. Mater. Electron.*, 2018, **10**, 1-12

47. A. Chaudhary, A. Mohammad and S. M. Mobin, *Mater. Sci. Eng: B*, 2018, **227**, 136-144.

48. T. Zhang, H. Zhu and J. P. Croué, *Environ. Sci. Technol.* 2013, **47**, 2784-2791.

49. H. Mehrizadeh, A. Niaei, H. H. Tseng, D. Salari and A. Khataee, *J. Photochem. Photobiol. A*, 2017, **332**, 188-195.

50. M. Wang, L. Sun, J. Cai, P. Huang, Y. Su and C. Lin, *J. Mater. Chem. A*, 2013, **1**, 12082-12087.

51. K. H. Wang, J.-M. Jehng, Y. H. Hsieh and C. Y. Chang, *J Hazard Mater.,* 2002, **90**, 63-75.

52. M. Yazdanbakhsh, I. Khosravi, E. K. Goharshadi and A. Youssefi, *J Hazard Mater.,* 2010, **184**, 684-689.

53. E. L. Foletto, S. Battiston, J. M. Simões, M. M. Bassaco, L. S. F. Pereira, É. M. de Moraes Flores and E. I. Müller, *Microporous Mesoporous Mater.,* 2012, **163**, 29-33.

54. Z. Mousavi, F. Soofivand, M. Esmaeili-Zare, M. Salavati-Niasari and S. Bagheri, *Sci. Rep.*, 2016, **6**, 20071.

55. M. I. Omer, A. Elbadawi and O. Yassin, *J. Appl. Indus. Sci.*, 2013, **1**, 20-23.

56. R. S. Jack, G. A. Ayoko, M. O. Adebajo and R. L. Frost, *Environ. Sci. Pollut. Res. Int.,* 2015, **22**, 7439-7449.

57. M. R. Hoffmann, S. T. Martin, W. Choi and D. W. Bahnemann, *Chem. Rev.,*1995, **95**, 69-96.

58. R. Dom, R. Subasri, K. Radha and P. H. Borse, *Solid State Commun.,* 2011, **151**, 470-473.

59. B. I. Kharisov, H. R. Dias and O. V. Kharissova, *Arab. J. Chem.,* 2014, **15**, 1-13.

60. M. Miyauchi, Z. Liu, Z. G. Zhao, S. Anandan and K. Hara, *Chem. Comm.*, 2010, **46**, 1529-1531.

61. M. Fukushima, K. Tatsumi and K. Morimoto, *Environ. Sci. Technol.,*2000, **34**, 2006-

2013.

62. C. Byrne, G. Subramanian and S. C. Pillai, *J. Environ. Chem. Eng.*, 2017, **1**, 1-8

63. P. Baldrian, V. Merhautová, J. Gabriel, F. Nerud, P. Stopka, M. Hrubý and M. J. Beneš, *Appl. Catal. B Environ.,* 2006, **66**, 258-264.

64. D. Arifin, V. J. Aston, X. Liang, A. H. McDaniel and A. W. Weimer, *Energy Environ. Sci.,* 2012, **5**, 9438-9443.

65. K. T. Lee, X. F. Chuah, Y. C. Cheng and S.-Y. Lu, *J. Mater. Chemi. A.*, 2015, **3**, 18578-18585.

66. T. B. Nguyen and R. A. Doong, *RSC Advances*, 2017, **7**, 50006-50016.

67. P. F. Newhouse and B. A. Parkinson, *J. Mater. Chemi. A.*, 2015, **3**, 5901-5907.

68. S. Navalon, A. Dhakshinamoorthy, M. Álvaro and H. Garcia, *ChemSusChem*, 2013, **6**, 562-577.

69. J. Marco, J. Gancedo, M. Gracia, J. Gautier, E. Rios and F. Berry, *J. Solid State Chem.,* 2000, **153**, 74-81.

70. B. Cui, H. Lin, Y. Z. Liu, J. B. Li, P. Sun, X. C. Zhao and C. J. Liu, *J. Phys. Chem. C.,* 2009, **113**, 14083-14087.

71. R. Sharma, S. Bansal and S. Singhal, *RSC Advances*, 2015, **5**, 6006-6018.

72. M. Dhiman, R. Sharma, V. Kumar and S. Singhal, *Ceram. Int.,* 2016, **42**, 12594-12605.

73. F. Fang, L. Chen, Y.-B. Chen and L. M. Wu, *J. Phys. Chem. C.,* 2010, **114**, 2393-2397.

74. G. Mathubala, A. Manikandan, S. A. Antony and P. Ramar, *J. Mol. Struct.,* 2016, **1113**, 79-87.

75. M. Shen, L. Fu, J. Tang, M. Liu, Y. Song, F. Tian, Z. Zhao, Z. Zhang and D. D. Dionysiou, *J Hazard. Mater*., 2018, **350**, 1-9.

76. S. Chakrabarty, A. Mukherjee and S. Basu, *ACS Sustain. Chem. Eng.,* 2018, 6, 5238–5247.

77. B. Safizade, S. Masoudpanah, M. Hasheminiasari and A. Ghasemi, *RSC Advances*, 2018, **8**, 6988-6995.

78. H. Li, Z. Sun, Y. Tian, G. Cui and S. Yan, *RSC Advances*, 2015, **5**, 79765-79773.

79. R. Shao, L. Sun, L. Tang and Z. Chen, *Chem. Eng. J.*, 2013, **217**, 185-191.

80. J. Xing, W. Q. Fang, H. J. Zhao and H. G. Yang, *Chem. Asian J.,* 2012, **7**, 642-657.

81. D. Voiry, H. S. Shin, K. P. Loh and M. Chhowalla, *Nat. Rev. Chem.,* 2018, **1**, 0105.

82. A. J. Esswein and D. G. Nocera, *Chem. Rev.*, 2007, **107**, 4022-4047.

83. A. Steinfeld, S. Sanders and R. Palumbo, *Solar Energy*, 1999, **65**, 43-53.

84. C. H. Chen, Y. H. Liang and W.-D. Zhang, *J Alloys Compd.,* 2010, **501**, 168-172.

85. G. Lu and S. Li, *Int. J. Hydrog. Energy.,*1992, **17**, 767-770.

86. R. Dom, A. S. Chary, R. Subasri, N. Y. Hebalkar and P. H. Borse, *Int. J. Energy Res.,* 2015, **39**, 1378-1390.

87. S. Saadi, A. Bouguelia and M. Trari, *Renewable Energy*, 2006, **31**, 2245-2256.

88. Y. Bessekhouad and M. Trari, *Int. J. Hydrog. Energy.,* 2002, **27**, 357-362.

89. A. Andreev, V. Idakiev, D. Mihajlova and D. Shopov, *Appl. Catal.,* 1986, **22**, 385-387.

90. A. Boudjemaa, R. Bouarab, S. Saadi, A. Bouguelia and M. Trari, *Appl. Energy.*, 2009, **86**, 1080-1086.

91. B. B. Kale, J. O. Baeg, S. M. Lee, H. Chang, S. J. Moon and C. W. Lee, *Adv. Funct. Mater.,* 2006, **16**, 1349-1354.

92. I. Sullivan, B. Zoellner and P. A. Maggard, *Chem. Mater.,* 2016, **28**, 5999-6016.

93. P. Akhter, M. A. Farkhondehfal, S. Hernández, M. Hussain, A. Fina, G. Saracco, A. U.

Khan and N. Russo, *J. Environ. Chem. Eng.*, 2016, **4**, 3934-3953.

94. J. Low, B. Cheng and J. Yu, *Appl. Surf. Sci.,* 2017, **392**, 658-686.

95. V. P. Indrakanti, J. D. Kubicki and H. H. Schobert, *Energy Environ. Sci.,* 2009, **2**, 745-758.

96. C. D. Windle and R. N. Perutz, *Coord. Chem. Rev.,*2012, **256**, 2562-2570.

97. J. Byun, W. Huang, D. Wang, R. Li and K. A. Zhang, *Angew. Chem. Int. Ed.,* 2018, **57**, 2967-2971.

98. C. S. Diercks, Y. Liu, K. E. Cordova and O. M. Yaghi, *Nat. Mater.*, 2018, 1-6.

99. B. Gholamkhass, H. Mametsuka, K. Koike, T. Tanabe, M. Furue and O. Ishitani, *Inorg. Chem.* 2005, **44**, 2326-2336.

100. S. Wang, Z. Ding and X. Wang, *Chem. Commun.*, 2015, **51**, 1517-1519.

101. X. Limei, Z. Fenghua, C. Bin and B. Xuefeng, Proceeding CDCIEM '11: Proceedings of the 2011 International Conference on Computer Distributed Control and Intelligent Environmental Monitoring, 2011, 2153-2156.

102. W. Jiang, X. Yin, F. Xin, Y. Bi, Y. Liu and X. Li, *Appl. Surf. Sci.,* 2014, **288**, 138-142.

103. J. Guo, K. Wang and X. Wang, *Catal. Sci. Technol.,* 2017, **7**, 6013-6025.

104. Z. Wang, M. Jiang, J. Qin, H. Zhou and Z. Ding, *Phys. Chem. Chem. Phys.,*2015, **17**, 16040-16046.

105. S. Wang, Y. Hou and X. Wang, *ACS Appl. Mater. Interfaces.,*2015, **7**, 4327-4335.

106. M. Jiang, Y. Gao, Z. Wang and Z. Ding, *Appl. Catal. B Environ.,* 2016, **198**, 180-188.

107. C. Gao, Q. Meng, K. Zhao, H. Yin, D. Wang, J. Guo, S. Zhao, L. Chang, M. He and Q. Li, *Adv. Mater.*, 2016, **28**, 6485-6490.

108. R. Dillert, D. H. Taffa, M. Wark, T. Bredow and D. W. Bahnemann, *APL Materials*,

2015, **3**, 104001.

109. H. Yang, Y. Mao, M. Li, P. Liu and Y. Tong, *New J. Chem.,* 2013, **37**, 2965-2968.

110. D. Hong, Y. Yamada, M. Sheehan, S. Shikano, C.-H. Kuo, M. Tian, C.-K. Tsung and S. Fukuzumi, *ACS Sustain. Chem. Eng.,* 2014, **2**, 2588-2594.

111. T. Hisatomi, J. Kubota and K. Domen, *Chem. Soc. Rev.*, 2014, **43**, 7520-7535.

112. M. Shahid, L. Jingling, Z. Ali, I. Shakir, M. F. Warsi, R. Parveen and M. Nadeem, *Mater. Chem. Phy.*, 2013, **139**, 566-571.

113. A. A. Tahir and K. U. Wijayantha, *J. Photochem. Photobiol.,* 2010, **216**, 119-125.

114. A. Usujima, S. Takeuchi, S. Endo and T. Irie, *Jpn. J. Appl. Phys.,* 1981, **20**, L505.

115. F. Cerrina, I. Abbati, L. Braicovich, F. Levy and G. Margaritondo, *Solid State Commun.* 1978, **26**, 99-102.

116. B.Scrosati, L. Fornarini, G. Razzini and L. Bicelli, *J. Electrochem. Soc.,* 1985, **132**, 593-598.

117. V. V. Todkar, R. S. Mane, C. D. Lokhande, S.-H. Lee and S.-H. Han, *Electrochim. Acta.,* 2006, **51**, 4674-4679.

118. Q. Wang, B. Liu, X. Wang, S. Ran, L. Wang, D. Chen and G. Shen, *J. Mater. Chem.,* 2012, **22**, 21647-21653.

119. M. A. Alpuche Aviles and Y. Wu, *J. Am. Chem. Soc.,* 2009, **131**, 3216-3224.

120. A. Walsh, K. S. Ahn, S. Shet, M. N. Huda, T. G. Deutsch, H. Wang, J. A. Turner, S.-H. Wei, Y. Yan and M. M. Al-Jassim, *Energy Environ. Sci.,* 2009, **2**, 774-782.

121. N. Guijarro, P. Bornoz, M. Prevot, X. Yu, X. Zhu, M. Johnson, X. Jeanbourquin, F. Le Formal and K. Sivula, *Sus. Energy. Fuels*, 2018, **2**, 103-117.

122. S. Chandrasekaran, W. M. Choi, J. S. Chung, S. H. Hur and E. J. Kim, *Mater. Lett.*, 2014,

136, 118-121.

123. W. Zhong, J. Chen, P. Zhang, L. Deng, L. Yao, X. Ren, Y. Li, H. Mi and L. Sun, *J. Mater. Chem. A.*, 2017, **5**, 16605-16610.

124. P. K. Boruah, S. Szunerits, R. Boukherroub and M. R. Das, *Chemosphere*, 2018, **191**, 503-513.

125. X. Cao, L. Gu, X. Lan, C. Zhao, D. Yao and W. Sheng, *Mater. Chem. Phys.,*2007, **106**, 175-180.

126. S. Mahalingam and Y.-H. Ahn, *New J. Chem.,* 2018, **42**, 4372-4383.

127. D. Mehandjiev, A. Naydenov and G. Ivanov, *Appl. Catal.,* 2001, **206**, 13-18.

128. M. J. Muñoz□Batista, D. Motta Meira, G. Colón, A. Kubacka and M. Fernández□García, *Angew. Chem. Int. Ed.,* 2018, **57**, 1199-1203.

129. J. Li, Z. Liu and Z. Zhu, *Appl. Surf. Sci.*, 2014, **320**, 146-153.

130. J. Li, Q. Xiao, L. Li, J. Shen and D. Hu, *Appl. Surf. Sci.*, 2015, **331**, 108-114.

131. L. Huang, S. Chu, J. Wang, F. Kong, L. Luo, Y. Wang and Z. Zou, *Catal. Today.,* 2013, **212**, 81-88.

132. S. Wang, B. Y. Guan and X. W. Lou, *J. Am. Chem. Soc.,* 2018, 140, 5037–5040.

133. Z. Chen, D. Li, W. Zhang, Y. Shao, T. Chen, M. Sun and X. Fu, *J. Phys. Chem. C.,* 2009, **113**, 4433-4440.

134. M. Sundararajan, L. John Kennedy, P. Nithya, J. Judith Vijaya and M. Bououdina, *J. Phys. Chem. Solids.,* 2017, **108**, 61-75.

135. C. J. Chang, Z. Lee, M. Wei, C. C. Chang and K. W. Chu, *Int. J. Hydrog. Energy.,* 2015, **40**, 11436-11443.

136. A. Borhan, P. Samoila, V. Hulea, A. R. Iordan and M. N. Palamaru, *J Taiwan Inst Chem*

Eng., 2014, **45**, 1655-1660.

137. Y. Lin, S. Lin, M. Luo and J. Liu, *Mater. Lett.*, 2009, **63**, 1169-1171.

138. G. Huang and Y. Zhu, *J. Phys. Chem. C.,* 2007, **111**, 11952-11958.

139. S. Wang, B. Guan and X. D. Lou, *Energy Environ. Sci.*, 2018, **11**, 306-310.

140. X. Xu, A. K. Azad and J. T. S. Irvine, *Catal. Today., 2013,* **199**, 22-26.

141. C. Feng, W. J. Yin, J. Nie, X. Zu, M. N. Huda, S. H. Wei, M. M. Al-Jassim, J. A. Turner and Y. Yan, *Appl. Phys. Lett.,* 2012, **100**, 023901.

142. M. Woodhouse, G. S. Herman and B. A. Parkinson, *Chemistry of Materials*, 2005, **17**, 4318-4324.

143. M. Woodhouse and B. A. Parkinson, *Chem. Mater.*, 2008, **20**, 2495-2502.

144. C. Miao, S. Ji, G. Xu, G. Liu, L. Zhang and C. Ye, *ACS Appl. Mater. Interfaces.,* 2012, **4**, 4428-4433.

145. M. Aresta, A. Dibenedetto and A. Angelini, *Chem. Rev.,* 2013, **114**, 1709-1742.

146. S. Zhou, Y. Liu, J. Li, Y. Wang, G. Jiang, Z. Zhao, D. Wang, A. Duan, J. Liu and Y. Wei, *Appl. Catal. B Environ.,* 2014, **158**, 20-29.

147. H. Hamad, M. A. El-Latif, A. E.-H. Kashyout, W. Sadik and M. Feteha, *New J. Chem.,* 2015, **39**, 3116-3128.

148. Y. Yao, J. Qin, H. Chen, F. Wei, X. Liu, J. Wang and S. Wang, *J Hazard. Mater.,* 2015, **291**, 28-37.

149. H. S. Kim, D. Kim, B. S. Kwak, G. B. Han, M. H. Um and M. Kang, *Chem. Eng. J.,* 2014, **243**, 272-279.

150. C. J. Chang, Z. Lee, K. W. Chu and Y. H. Wei, *J Taiwan Inst Chem Eng.,* 2016, **66**, 386-393.

151. Y. Liu, Y. Song, Y. You, X. Fu, J. Wen and X. Zheng, *J. Saudi. Chem. Soc.*, 2018, 22, 439-448.

152. S. Huang, Y. Xu, M. Xie, H. Xu, M. He, J. Xia, L. Huang and H. Li, *Colloid Surf A Physicochem Eng Asp.,* 2015, **478**, 71-80.

153. J. Zeng, T. Song, M. Lv, T. Wang, J. Qin and H. Zeng, *RSC Advances*, 2016, **6**, 54964-54975.

154. K. J. McDonald and K. S. Choi, *Chem. Mater.,* 2011, **23**, 4863-4869.

155. Z. Luo, C. Li, D. Zhang, T. Wang and J. Gong, *Chem. Commun.*, 2016, **52**, 9013-9015.

156. Q. Liu, F. Cao, F. Wu, W. Tian and L. Li, *RSC Advances*, 2015, **5**, 79440-79446.

157. K. Li, X. An, K. H. Park, M. Khraisheh and J. Tang, *Catal. Today*, 2014, **224**, 3-12.

158. H. Q. Xu, J. Hu, D. Wang, Z. Li, Q. Zhang, Y. Luo, S.-H. Yu and H.-L. Jiang, *J. Am. Chem Soc.* 2015, **137**, 13440-13443.

159. S. Tebani, N. Nasrallah, B. Bellal, A. Chergui, M. Trari and R. Maachi, *Arab. J.. Sci. Eng.*, 2017, **42**, 2397-2402.

160. G. Song, X. Wu, F. Xin and X. Yin, *J. Nanosci. Nanotechnol.*, 2017, **17**, 2438-2446.

161. A. Arango-Diaz, J. Cecilia, J. Marrero-Jerez, P. Nuñez, J. Jiménez-Jiménez and E. Rodríguez-Castellón, *Ceram Int.,* 2016, **42**, 7462-7474.

162. G. Song, F. Xin and X. Yin, *J. Colloid Interface Sci.,* 2015, **442**, 60-66.

163. J. Liu, D. Wang, M. Wang, D. Kong, Y. Zhang, J. F. Chen and L. Dai, *Chem. Eng. Technol.,* 2016, **39**, 891-898.

164. E. L. Foletto, S. Battiston, J. M. Simões, M. M. Bassaco, L. S. F. Pereira, É. M. de Moraes Flores and E. I. Müller, *Micropor. Mesopor. Mat.,* 2012, **163**, 29-33.

165. C. G. Anchieta, D. Sallet, E. L. Foletto, S. S. Da Silva, O. Chiavone-Filho and C. A. do

Nascimento, *Ceram Int.*, 2014, **40**, 4173-4178.

166. B. Qiu, Y. Deng, M. Du, M. Xing and J. Zhang, *Sci. Rep.*, 2016, **6**, 29099-29106.

167. Q. Liu, D. Wu, Y. Zhou, H. Su, R. Wang, C. Zhang, S. Yan, M. Xiao and Z. Zou, *ACS Appl. Mater. Interfaces.,* 2014, **6**, 2356-2361.

168. L. Yao, J. Yang, P. Zhang and L. Deng, *Bioresource Technology*, 2018, **256**, 208-215.

169. N. Pang, F. Ye and Y. Jiang, *Materials Research Express*, 2017, **4**, 055013.

170. J. Jiang, W. Shi, F. Guo and S. Yuan, *Inorg Chem Front.* 2018. doi: 10.1039/C8QI00290H

171. P. Zhou, Z. Li and Z. Zou, *Curr Inorg Chem.,* 2012, **2**, 184-193.

172. P. Jing, J. Li, L. Pan, J. Wang, X. Sun and Q. Liu, *J Hazard. Mater.,* 2015, **284**, 163-170.

173. P. Jing, J. Du, J. Wang, W. Lan, L. Pan, J. Li, J. Wei, D. Cao, X. Zhang and C. Zhao, *Nanoscale*, 2015, **7**, 14738-14746.

174. E. Skliri, J. Miao, J. Xie, G. Liu, T. Salim, B. Liu, Q. Zhang and G. S. Armatas, *Appl. Catal. B Environ.,* 2018, **227**, 330-339.

175. P. Zhang, Y. Shi, M. Chi, J.-N. Park, G. D. Stucky, E. W. McFarland and L. Gao, *Nanotechnol.*, 2013, **24**, 345704.

176. J. Rosen, G. S. Hutchings and F. Jiao, *J. Am. Chem. Soc.*, 2013, **135**, 4516-4521.

177. H. Long, B. Ren, J. Li, L. Zhang, L. Tan, L. Dong and Z. Liu, *J Alloys Compd.,* 2017, **720**, 437-444.

178. E. Pervaiz, M. S. A. Virk, A. K. Tareen, B. Zhang, Q. Zhao, Z. Wang and M. Yang, *Nanotechnol.*, 2018, **29**, 215710.

179. Z. Peng, S. Yifeng, C. Miaofang, P. Jung-Nam, D. S. Galen, W. M. Eric and G. Lian, *Nanotechnol.*, 2013, **24**, 345704.

180. W. Meng, F. Li, D. G. Evans and X. Duan, *J. Porous Mat.,* 2004, **11**, 97-105.

181. S. T. Liu, A. B. Zhang, K. K. Yan, Y. Ye and X.-G. Chen, *Sep. Purif. Technol.,* 2014, **135**, 35-41.

182. P. W. Menezes, A. Indra, N. R. Sahraie, A. Bergmann, P. Strasser and M. Driess, *ChemSusChem*, 2015, **8**, 164-171.

183. A. Kalam, A. G. Al-Sehemi, M. Assiri, G. Du, T. Ahmad, I. Ahmad and M. Pannipara, *Results in Physics*, 2018, **8**, 1046-1053.

184. S. D. Jadhav, P. P. Hankare, R. P. Patil and R. Sasikala, *Mater. Lett.,* 2011, **65**, 371-373.

185. J. H. Kim, J. H. Kim, J. W. Jang, J. Y. Kim, S. H. Choi, G. Magesh, J. Lee and J. S. Lee, *Adv. Energy Mater.,* 2015, **5**, 1401933.

186. R. C. C. Costa, M. d. F. F. Lelis, L. C. A. Oliveira, J. D. Fabris, J. D. Ardisson, R. R. V. A. Rios, C. N. Silva and R. M. Lago, *Catal. Commun. ,*2003, **4**, 525-529.

187. K. Wang, L. Yu, S. Yin, H. Li and H. Li, *Pure Appl. Chem.*, 2009, **81**, 2327-2335.

188. S. Hussain, A. Waleed, M. M. Tavakoli, Z. Wang, S. Yang, Z. Fan and M. A. Nadeem, *ACS Appl. Mater. Interfaces.,* 2016, **8**, 35315-35322.

189. P. Kumar, C. Joshi, A. Barras, B. Sieber, A. Addad, L. Boussekey, S. Szunerits, R. Boukherroub and S. L. Jain, *Appl. Catal. B Environ.,* 2017, **205**, 654-665.

190. A. Sutka, M. Millers, M. Vanags, U. Joost, M. Maiorov, V. Kisand, R. Pärna and I. Juhnevica, *Res. Chem. Intermed.,* 2015, **41**, 9439-9449.

191. H. Liu, Z. Zhang, J. Meng and J. Zhang, *Mol Catal*, 2017, **430**, 9-19.

192. S. K. Sampath and J. F. Cordaro, *J. Am. Ceram. Soc.,* 1998, **81**, 649-654.

193. S. C. Yan, S. X. Ouyang, J. Gao, M. Yang, J. Y. Feng, X. X. Fan, L. J. Wan, Z. S. Li, J. H. Ye and Y. Zhou, *Angew. Chem. Int. Ed.,* 2010, **122**, 6544-6548.

194. W. Yin, S. Hao and H. Cao, *RSC Advances*, 2017, **7**, 4062-4069.

195. X. Sun, S. Wang, C. Shen and X. Xu, *ChemCatChem*, 2016, **8**, 2289-2295.

196. R. A. Candeia, M. I. B. Bernardi, E. Longo, I. M. G. Santos and A. G. Souza, *Mater. Lett.,* 2004, **58**, 569-572.

197. S. Ida, K. Yamada, T. Matsunaga, H. Hagiwara, Y. Matsumoto and T. Ishihara, *J. Am. Chem. Soc.,* 2010, **132**, 17343-17345.

198. J. Cao, T. Kako, P. Li, S. Ouyang and J. Ye, *Electrochem. Commun.,* 2011, **13**, 275-278.

199. M. G. Ahmed, T. A. Kandiel, A. Y. Ahmed, I. Kretschmer, F. Rashwan and D. Bahnemann, *J. Phys. Chem. C.,* 2015, **119**, 5864-5871.

200. R. A. Candeia, M. A. F. Souza, M. I. B. Bernardi, S. C. Maestrelli, I. M. G. Santos, A. G. Souza and E. Longo, *Ceram. Int.,* 2007, **33**, 521-525.

201. P. Borse, C. Cho, K. Lim, Y. Lee, T. Hong, J. Bae, E. Jeong, H. Kim and H. Kim, *J. Korean Phys. Soc.,* 2011, **58**, 1672-1676.

202. Y. Yang, Y. Jiang, Y. Wang, Y. Sun, L. Liu and J. Zhang, *Mater. Chem. Phys.*, 2007, **105**, 154-156.

203. S. W. Lee, J. Drwiega, D. Mazyck, C.-Y. Wu and W. M. Sigmund, *Mater. Chem. Phys.,* 2006, **96**, 483-488.

204. S. H. Hosseini, S. H. Mohseni, A. Asadnia and H. Kerdari, *J. Alloys Compd.,* 2011, **509**, 4682-4687.

205. M. Y. Rafique, P. Li-Qing, M. Z. Iqbal, Q. Hong-Mei, M. H. Farooq, G. Zhen-Gang and M. Tanveer, *Chin. Phys. B.,* 2013, **22**, 107101.

206. A. M. Jacintha, A. Manikandan, K. Chinnaraj, S. A. Antony and P. Neeraja, *J. Nanosci. Nanotechnol.,* 2015, **15**, 9732-9740.

207. X. Hou, J. Feng, X. Xu and M. Zhang, *J. Alloys Compd.,* 2010, **491**, 258-263.

208. G. Zhang, W. Xu, Z. Li, W. Hu and Y. Wang, *J. Magn. Magn. Mater.,* 2009, **321**, 1424-1427.

209. P. Cheng, C. Deng, M. Gu and W. Shangguan, *J. Mater. Sci.,* 2007, **42**, 9239-9244.

210. V. C. Srivastava, *J. Appl. Phys.,* 1969, **40**, 1017-1019.

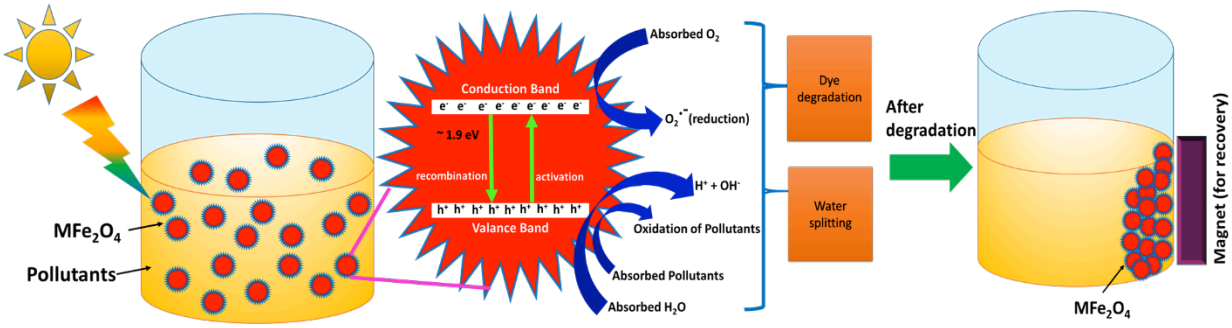

Fig. 1 Schematic of pollutant degradation and water splitting of spinel ferrite based photocatalysts under solar light irradiation. Where the mesoporous spinels were dispersed in reaction solution, the enlarged image shows the photocatalytic mechanism of dye degradation and hydrogen generation in photocatalyst dispersed system under light condition, finally the recovery of ferrite spinels using the bar magnet for further use.

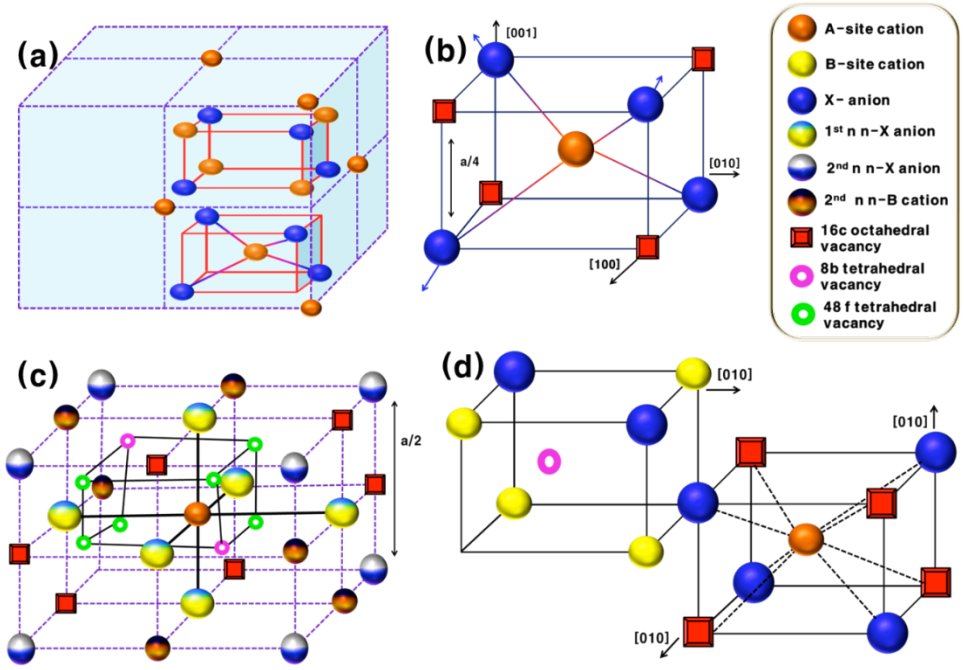

Fig. 2 Schematic of (a) spinel's of primitive tetragonal and cubic unit cells. The primitive cell contains two octants of the cubic unit cell. Atomic positions are exposed for the primitive unit cell only. Lattice arrangements and nearest neighbors for (b) A-site of the tetrahedral (8a), where the anion dilations are showed by solid blue colored arrows. (c) the octahedral B-site (16d), and (d) the tetrahedral anion X-site (32e), inspired by Ref[30]

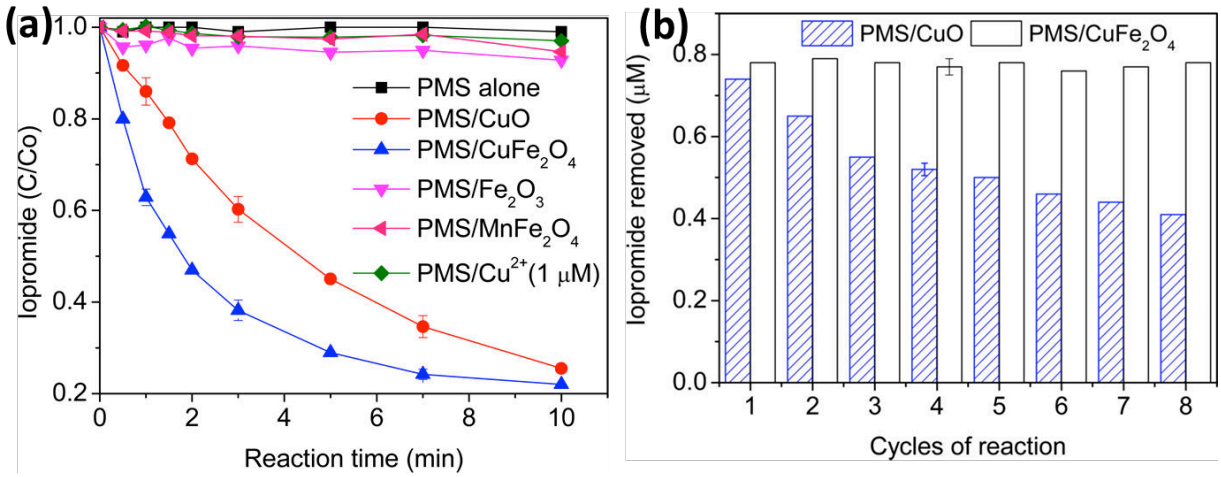

Fig. 3 (a) Degradation of Iopromide in peroxymonosulfate oxidation; Reaction Conditions: oxide dose = 100 mg L^{-1}, initial iopromide concentration = 1 μM, PMS dose = 20 μM, 10 mM tetraborate buffered pH 6.0, T = 20°C. Error bars represent standard deviations from triplicate experiments and (b) removal of Iopromide in repetitive batch catalytic reactions with the same spinel particles. Conditions: oxide dose = 100 mg L^{-1}, initial iopromide concentration in each cycle = 1 μM, PMS dose in each cycle = 20 μM, 10 mM tetraborate buffered pH 6.0, T = 20°C, at 10 min[48]. *Copyright permission@2013 from ACS.*

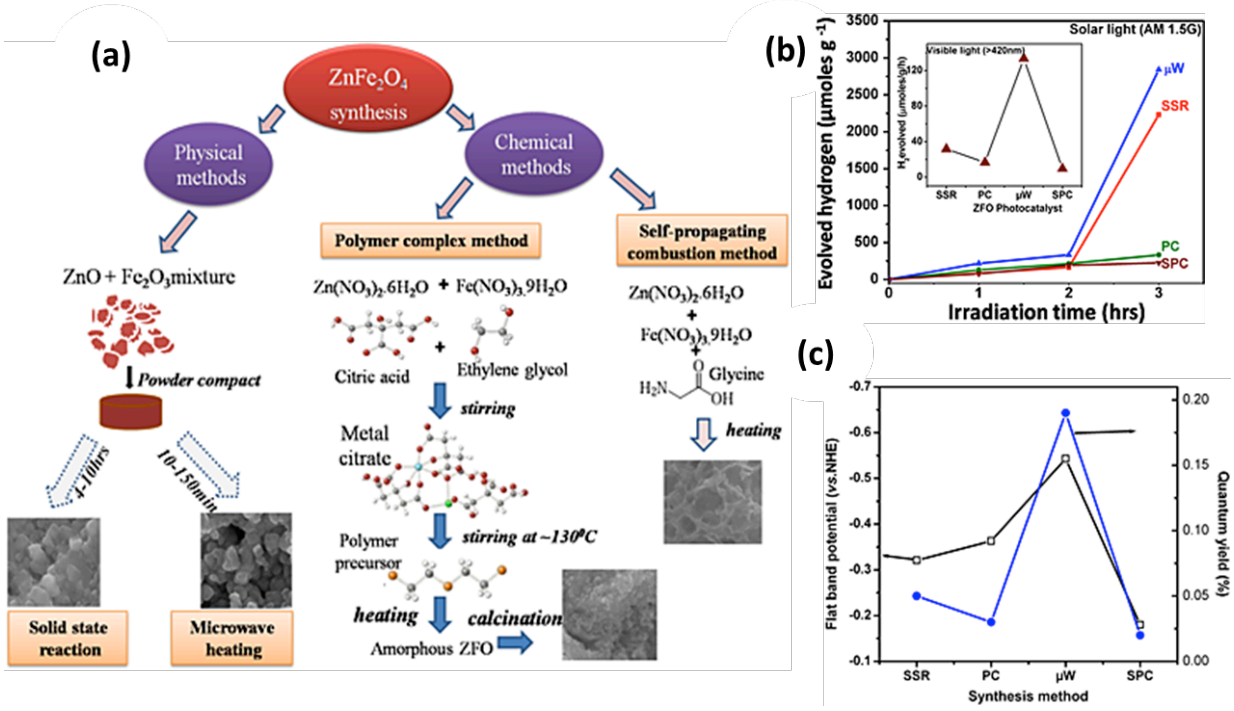

Fig. 4 (a) Schematic of synthesis approaches of spinel $ZnFe_2O_4$ (b) hydrogen evolution process of various $ZnFe_2O_4$ (ZFO) photocatalyst under solar simulator, inset shows the rate of hydrogen evolution under visible light ($\lambda = 420$ nm) (c) calculated flat-band potential and quantum yield of the ZFO photocatalysts with synthesis method[86]. *Copyright permission@2015 from Wiley*.

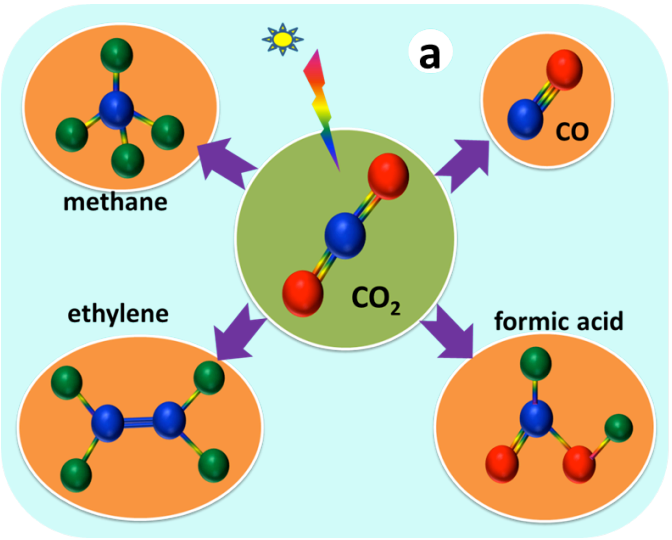

b

Reaction	E^{0}_{redox}, V vs. NHE
$2H^{+} + 2e^{-} \longrightarrow H_2$	-0.41
$H_2O \longrightarrow 1/2O_2 + 2H^{+} + 2e^{-}$	0.82
$CO_2 + e^{-} \longrightarrow CO_2^{\bullet-}$	-1.90
$CO_2 + H^{+} + 2e^{-} \longrightarrow HCO_2^{-}$	-0.49
$CO_2 + 2H^{+} + 2e^{-} \longrightarrow CO + H_2O$	-0.53
$CO_2 + 4H^{+} + 4e^{-} \longrightarrow HCHO + H_2O$	-0.48
$CO_2 + 6H^{+} + 6e^{-} \longrightarrow CH_3OH + H_2O$	-0.38
$CO_2 + 8H^{+} + 8e^{-} \longrightarrow CH_4 + 2H_2O$	-0.24

Fig. 5 (a) Schematic of hydrocarbon fuels generation from reduction of CO_2 and (b) reduction potentials (*vs.*NHE) of one, two, six and eight electrons involved certain reactions in CO_2 photoreduction at pH = 7[95]. *Copyright permission@**2009** from RSC*.

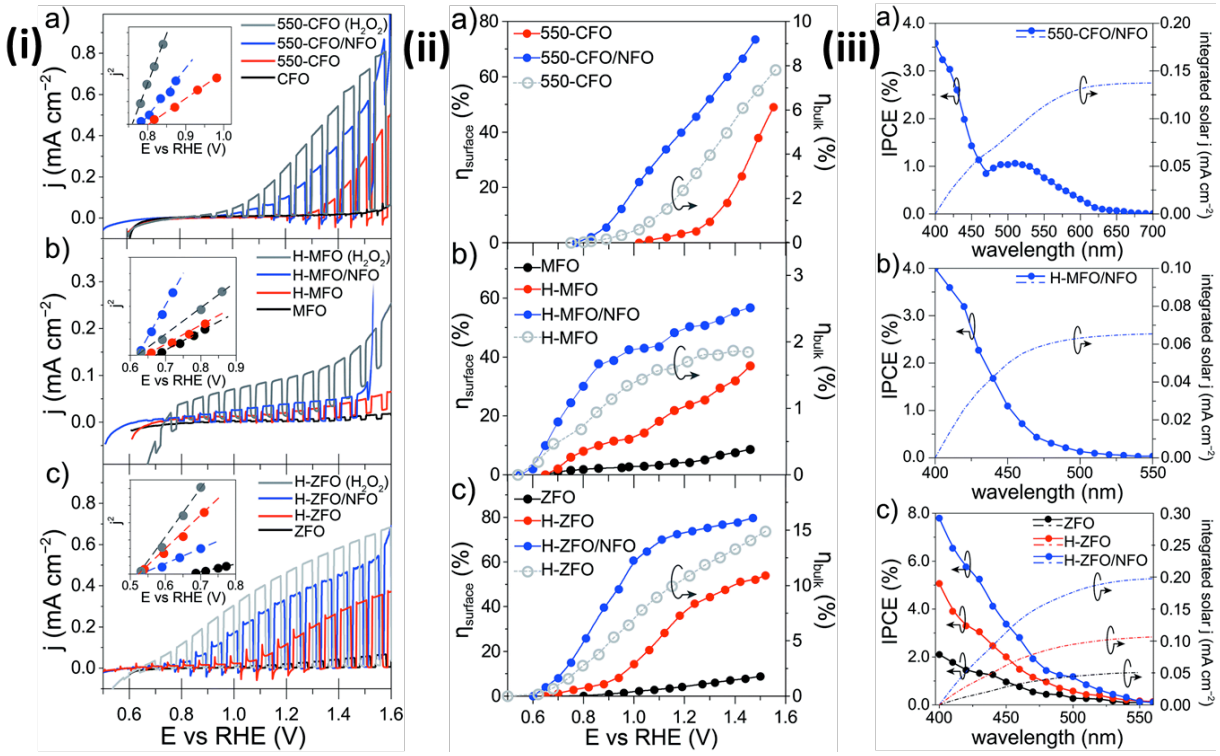

Fig. 6 (i) (a-c) Linear sweep voltammograms of (a) CFO, (b) MFO and (c) ZFO under 1 sun (AM 1.5G) illumination, insets are Butler plots. 1 M NaOH electrolyte used except for those measurements showed in grey as "(H_2O_2)" which were acquired in 1 M NaOH + 0.5 M H_2O_2 using a scan rate of 10 mV s^{-1}. (ii) Charge transfer yield ($\eta_{surface}$, left axis and full markers) and of charge separation (η_{bulk}, right axis and empty markers) determined for (a) CFO, (b) MFO and (c) ZFO. (iii) IPCE spectra of (a) 550-CFO/NFO recorded at 1.23 V *vs.* RHE, (b) H-MFO/NFO at 1.4 V *vs.* RHE and (c) ZFO at 1.1 V *vs.* RHE (left axis), including the integrated photocurrent (right axis)[121]. *Copyright permission@**2018** from ACS.*

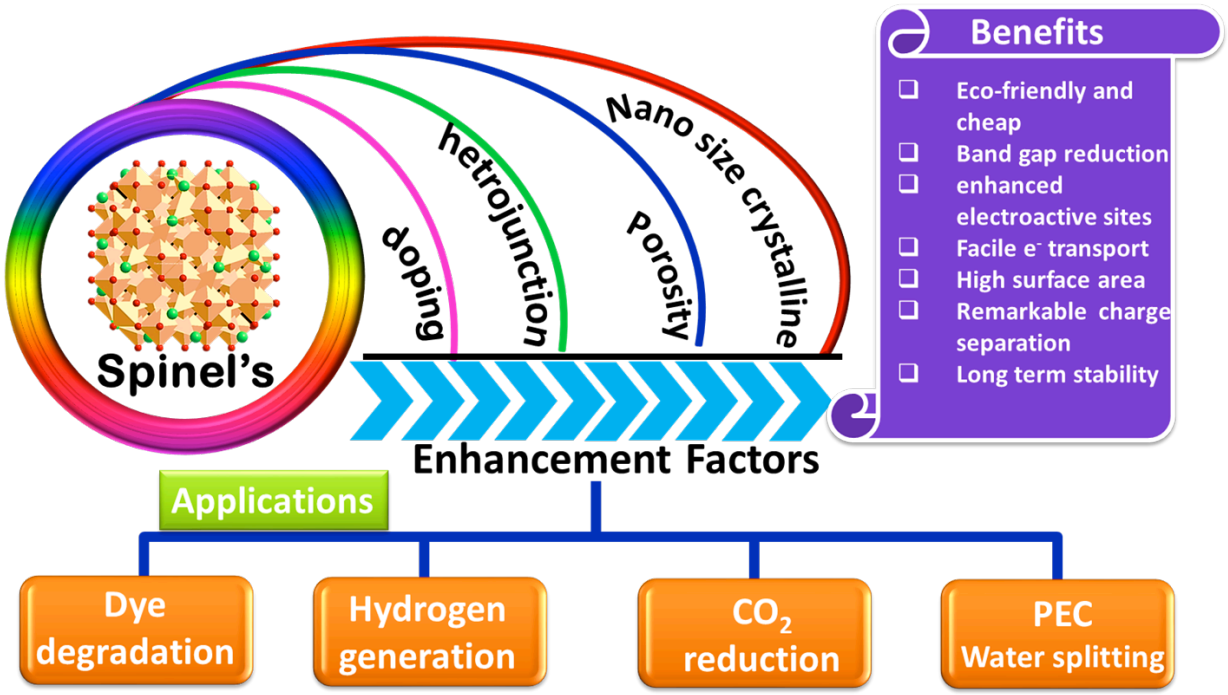

Fig. 7 Strategies to improve the performance of spinel photocatalysts

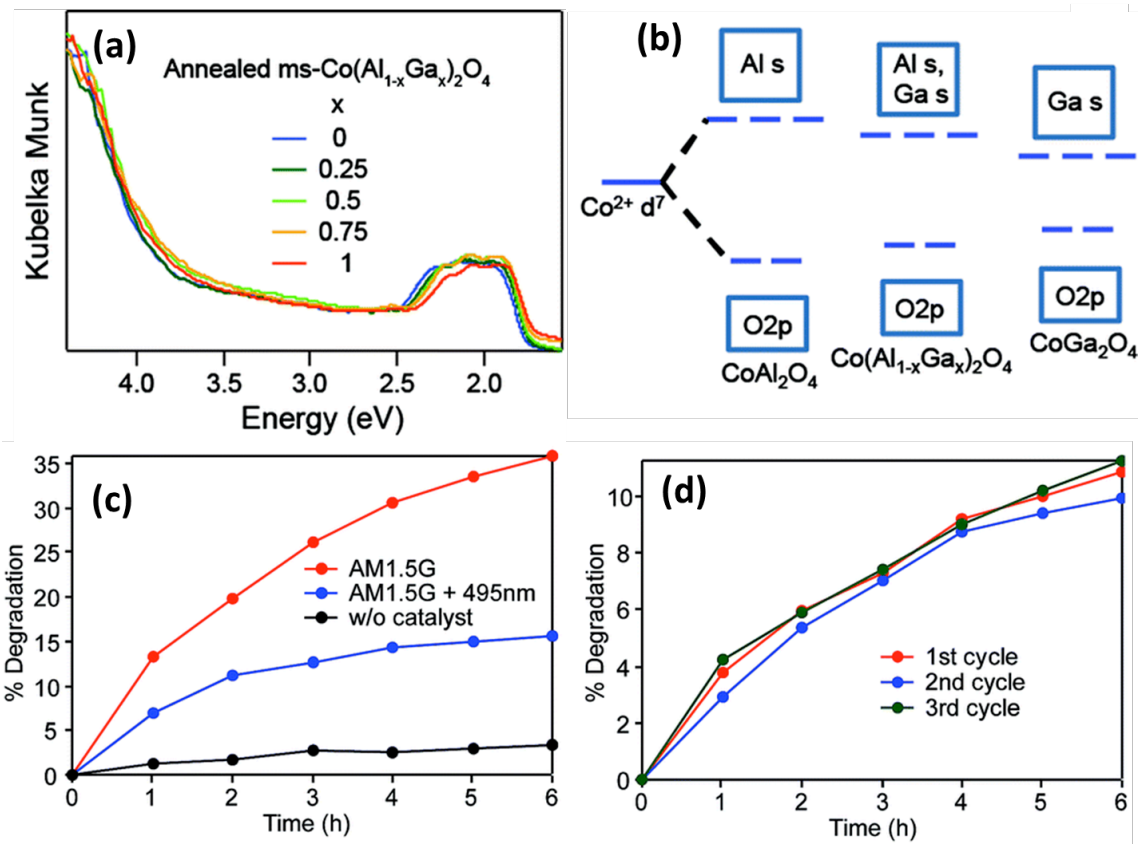

Fig. 8 Reflectance spectra of (a) ms-$Co(Al_{1-x}Ga_x)_2O_4$ annealed (1000 °C, 1 h) with varying *x*; i.e. prepared by for multi-source (ms) route (b) suggested band structure of $Co(Al_{1-x}Ga_x)_2O_4$ (c) photodegradation of methyl orange (MO) with annealed ms-$Co(Al_{0.5}Ga_{0.5})_2O_4$ at pH 3 under full spectrum simulated solar illumination (red, w/ AM1.5G filter) and visible light irradiation (blue) using a AM1.5G filter and a 495 nm long pass filter and (d) Recyclability result showing the photodegradation rate of MO at pH 3 under visible light was retained using the same annealed sample of ms-$Co(Al_{0.5}Ga_{0.5})_2O_4$ for 3 fresh MO solutions[16]. *Copyright permission@**2015** from RSC.*

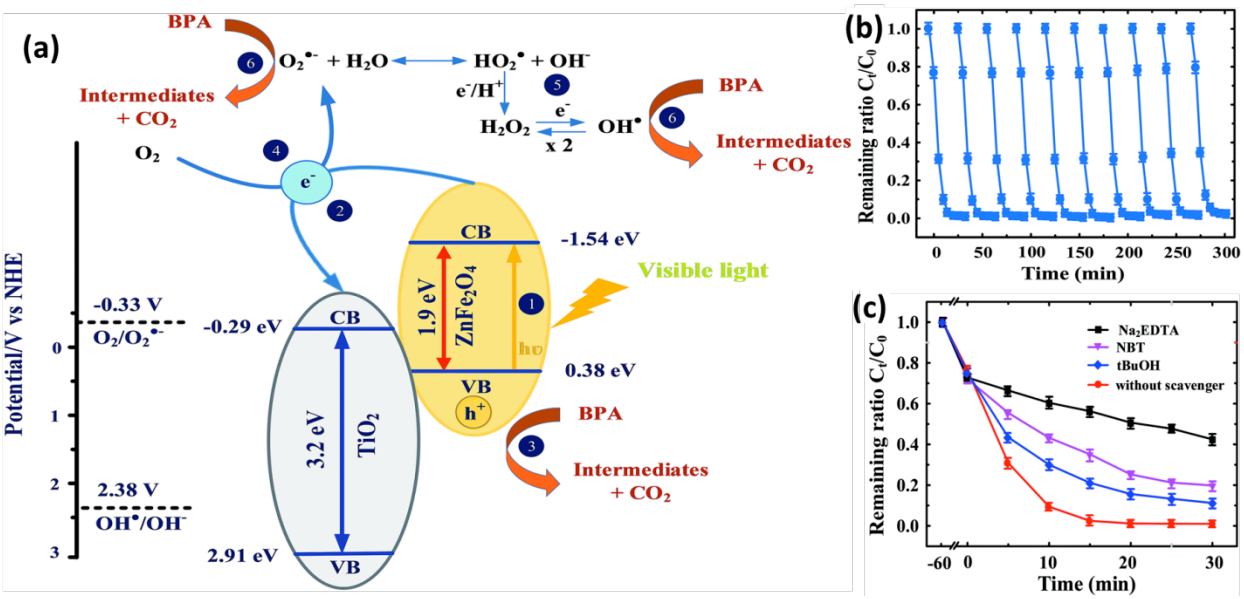

Fig. 9 (a) Schematic of visible-light-driven photodegradation of Bisphenol A by $ZnFe_2O_4$–TiO_2 under visible light irradiation. (b) The recyclability and (c) photocatalytic degradation of bisphenol A by 1 wt% $ZnFe_2O_4$–TiO_2 in the existence of 1 mM radical scavengers including *tert*-butanol (*t*-BuOH), nitroblue tetrazolium (NBT) and Na_2EDTA[66]. *Copyright permission@2017 from RSC.*

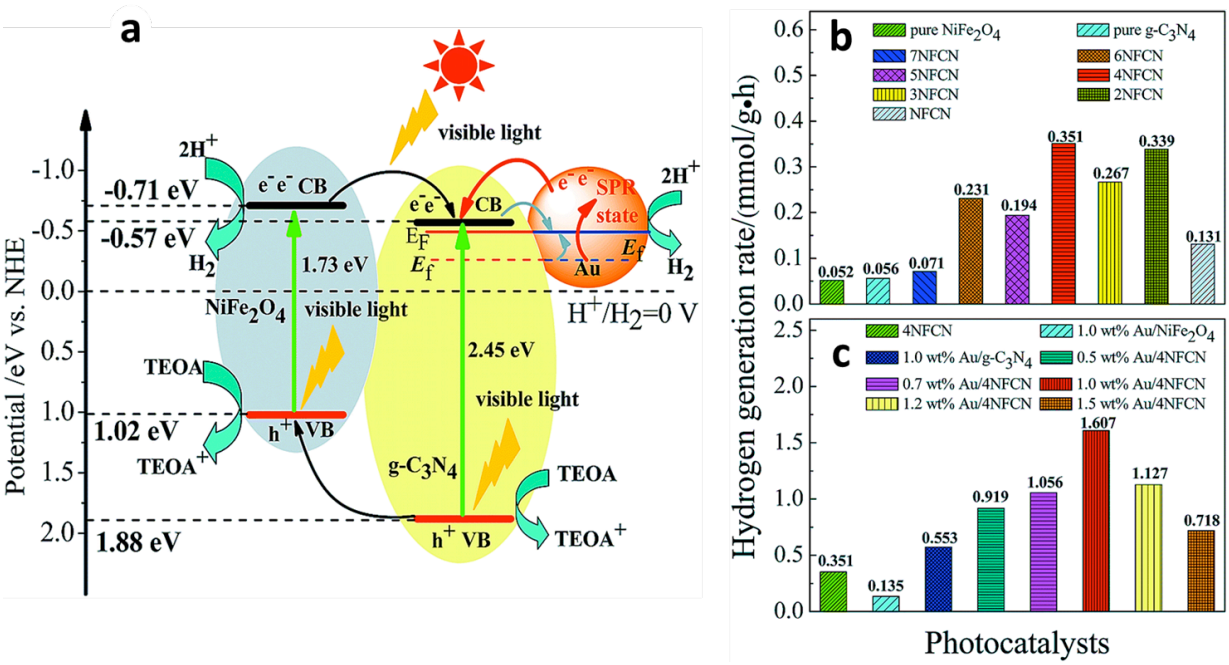

Fig. 10 (a) Photocatalytic hydrogen generation mechanism of Au/g-C_3N_4/$NiFe_2O_4$ photocatalysts and (b) hydrogen generation rate of pristine $NiFe_2O_4$, pristine g-C_3N_4 and $NiFe_2O_4$/g-C_3N_4 nanocomposites; (b) hydrogen generation rate different mass fraction of Au on g-C_3N_4/$NiFe_2O_4$ (light irradiation for 3 h)[153]. *Copyright permission@2016 from RSC.*

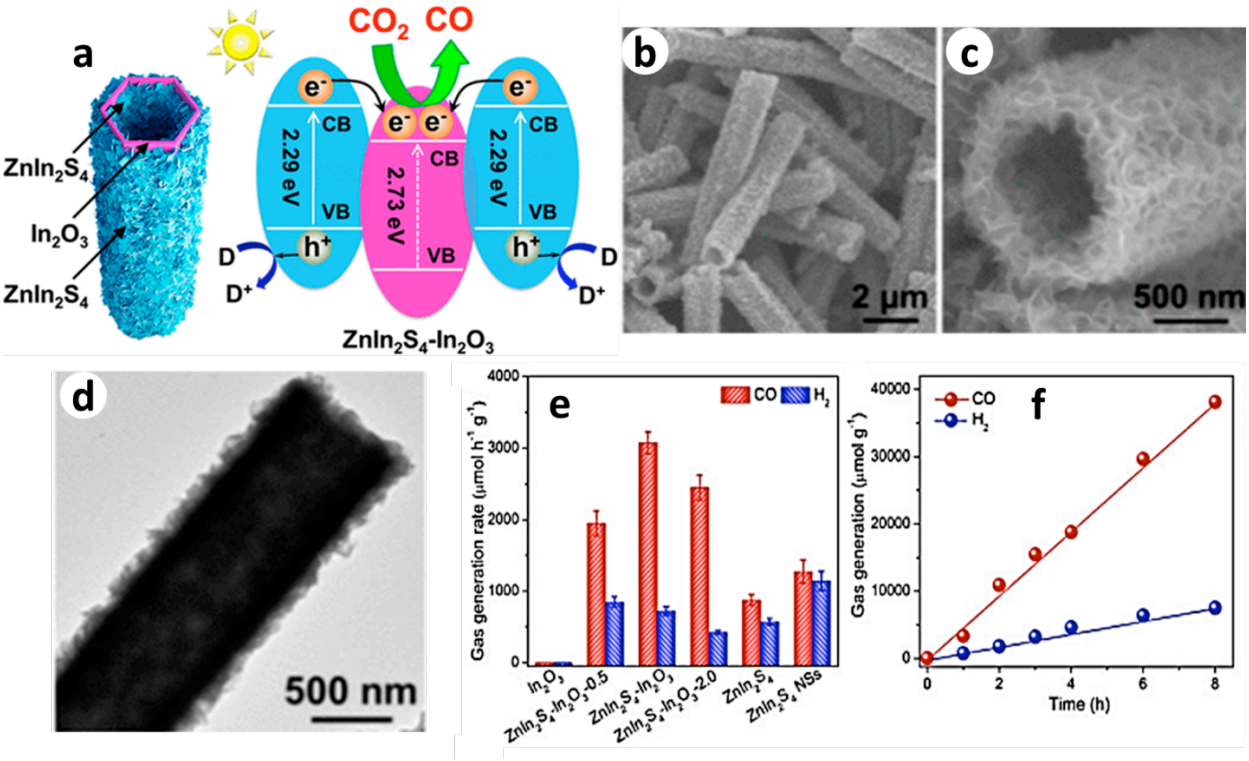

Fig. 11 (a) Schematic representation of photocatalytic CO_2 reduction mechanism by hetrostructured $ZnIn_2S_4$–In_2O_3 hierarchical tubes, (b-d) microscopic images of hierarchical microtubes and (e-f) CO_2 photoreduction activities of different photocatalysts and Time–yield plots of products respectively[132]. *Copyright permission@2018 from ACS.*

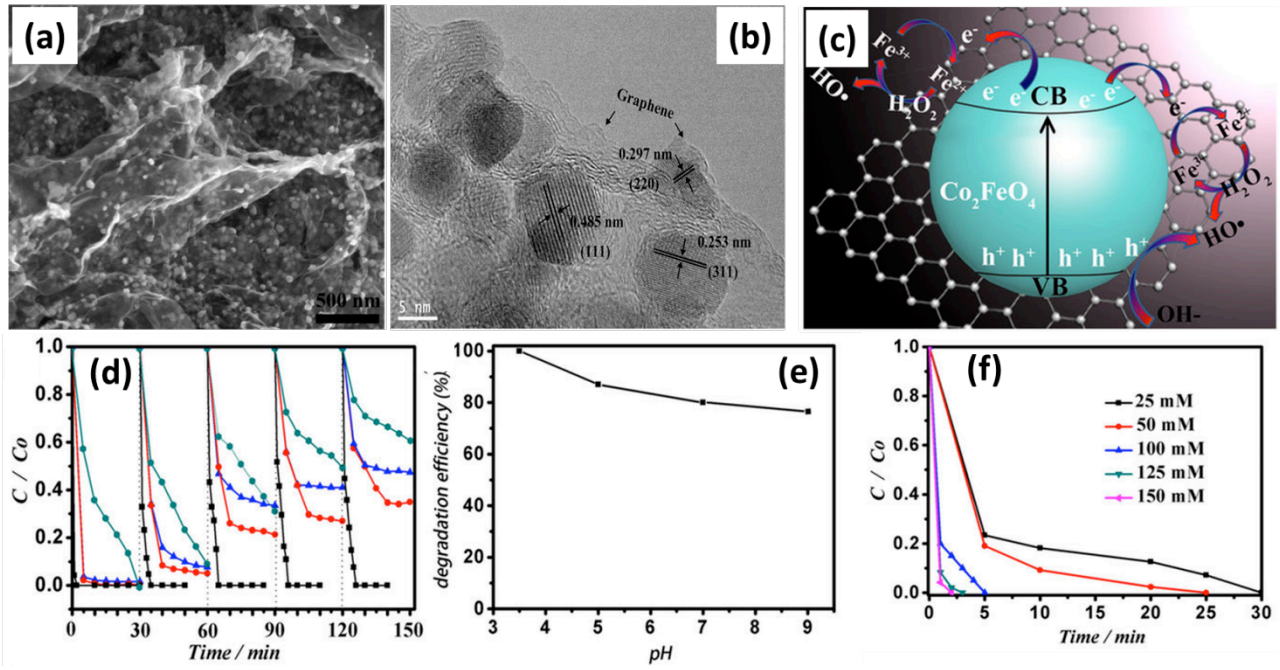

Fig. 12 (a,b) Transmission electron micrographs of $CoFe_2O_4$/Graphene composite (GAs) (c) Photo-Fenton reaction mechanism of $CoFe_2O_4$/GAs (d) Solar-driven degradation of methyl-orange (MO) cycle test; black line: $CoFe_2O_4$/GAs with H_2O_2 under irradiation; red line: $CoFe_2O_4$/GAs with H_2O_2 in the dark; blue line: $CoFe_2O_4$/GAs without H_2O_2 in the dark; dark cyan line: pure $CoFe_2O_4$ powders with H_2O_2 under irradiation) (70 mL MO, 10 mg/L, where 150 mM H_2O_2 (30 wt%), the initial pH was 3.5 used (e) pH effect on photodegradation efficiency of MO on $CoFe_2O_4$/GAs photocatalyst (70 mL MO, 10 mg/L; 150 mM H_2O_2 (30 wt%); t:30 min; the third cycle data) (f) H_2O_2 concentration effect on photodegradation efficiency of MO on $CoFe_2O_4$/GAs photocatalyst (70 mL MO, 10 mg/L; pH: 3.5; the third cycle data)[166]. *Copyright permission@2016 from Nature.*

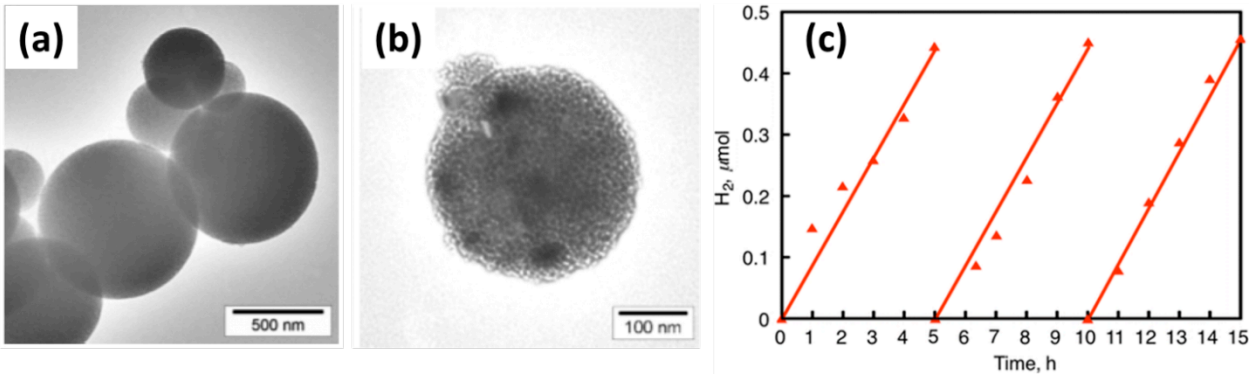

Fig. 13 (a-b) Transmission electron micrographs of mesoporous nickel ferrites (NF10b sample) and **(c)** H_2 evolution under visible light irradiation (Xe lamp, $\lambda > 420$ nm) of an aqueous solution (4.0 mL, pH 7.0) containing methanol (1.0 mL) and NF10b (2.0 mg, red triangles) in three repetitive analysis[110]. *Copyright permission@2014 from ACS.*